OPTICAL POLARIZATION CONTROL IN FREE SPACE AND THROUGH RANDOM MEDIA USING WAVEFRONT SHAPING

BY

SANTOSH TRIPATHI

DISSERTATION

Submitted in partial fulfillment of the requirements
for the degree of Doctor of Philosophy in Electrical and Computer Engineering
in the Graduate College of the
University of Illinois at Urbana-Champaign, 2013

Urbana, Illinois

Doctoral Committee:

Associate Professor Kimani C. Toussaint, Chair
Associate Professor Jonathan J. Makela
Professor Umberto Ravaioli
Professor José E. Schutt-Ainé

ABSTRACT

Light is widely used in areas such as optical communications, micro/nano fabrication, industrial process control, material characterization, and biomedical imaging. The usefulness of light in these areas depends on the dexterity with which the state of the optical field, defined by the spatio-temporal distribution of the field's phase, intensity, polarization and coherence, can be controlled and delivered to the required spatio-temporal position. In this thesis, we present two novel techniques to control the polarization of light, one for light propagating in free space and the other for light that is transmitted through highly scattering material. The former is useful in the characterization of materials and structures lying on the surface whereas the later, with further development, has potential to be useful in 3D IC fabrication/characterization, deep tissue imaging, and photodynamic therapy of diseases. The first technique relates to the generation of vector beams, which possess a spatially varying distribution of polarization according them with many interesting properties. However, the majority of techniques reported in the literature to generate vector beams employ interferometers, thereby limiting the stability of the beams generated. By using the polarization rotation behavior of nematic liquid crystal spatial light modulators (SLMs) and a specially designed optical setup, we develop a system that can generate a wide variety of vector beams without using interferometers. We also show that the diversity of polarization present in vector beams can be advantageously used in a variety of material characterization problems. Specifically, we show that the diversity of polarization can be used to expedite the characterization of thin films in ellipsometric measurements and improve the robustness of characterization in the measurement of the elements of the second-order nonlinear susceptibility tensor of single nanoparticles. The second technique relates to controlling the state of light transmitted through highly scattering media. In this regard, we introduce the concept of the vector transmission matrix (VTM) by generalizing the conventional transmission matrix. We develop a novel technique to measure the absolute value of VTM el-

ements and show that the randomness of the medium can be used as a resource in controlling the phase, amplitude and polarization of the transmitted light and demonstrate the first ever quantitative control over these parameters. The majority of our experiments in scattering media rely on the use of a phase-only SLM that we designed using Texas Instruments' DLP LightCrafter evaluation module which currently costs less than $600. It is well known that the spatially dependent modulation of an optical field's phase enables many novel applications; however, phase-only SLMs are expensive optical components and as a result are not yet widely used. The low-cost, phase-only SLM customized and presented in this thesis has the potential to change this situation thereby helping advancements in the field.

To all intrepid dreamers ...
for their dreams drive us forward

ACKNOWLEDGMENTS

I would like to thank Dr. Kimani C. Toussaint, my thesis adviser, for giving me an opportunity to work under his supervision. I would also like to thank my dissertation committee members Dr. Jonathan J. Makela, Dr. Umberto Ravaioli, and Dr. José E. Schutt-Ainé for their comments and suggestions. It was fun to be with the members of the Photonics Research of Bio/Nano Environments Laboratory for the last few years and I am thankful to all members—past and present—of the laboratory for their friendship.

TABLE OF CONTENTS

CHAPTER 1

INTRODUCTION

1.1 Motivation

Light is widely used in the characterization of materials and systems of biological and industrial importance [1–3]. In the semiconductor industry, it is used to measure the shape, size, and orientation of the fabricated micro/nano-structures in addition to measuring the properties of the materials from which the structures are fabricated [1, 4]. In biology, it has been used to characterize both structure [3] and function [2] of biological materials. The usefulness of light in these characterization problems depends upon the state of the light used [1, 2]; for example, optical coherence tomography (OCT) requires that an optical field of short coherence length be used [3], whereas stimulated emission depletion microscopy requires that an optical field with a donut-shaped intensity profile be used [2]. One of the properties of light affecting its state is polarization and, over the years, many characterization techniques, like ellipsometry and related polarimetry techniques [1, 4, 5], polarization-sensitive OCT [6], and polarization-sensitive digital holographic microscopy (DHM) [7], that rely on polarization have been developed. However, with a push toward a real-time characterization of biological and industrial systems and processes [1, 3], there is a general need to increase the speed at which these techniques can characterize the samples. One route to increasing the characterization speed can be to borrow the concept of using diversity of a resource to improve the system performance which is routinely used in communications [8–10]. For polarization based techniques, a natural choice is to create a diversity in polarization. One approach to achieving this is through the use of vector beams, which are beamlike solutions of Maxwell's equations that exhibit spatially nonuniform polarization across their cross-section [11, 12]. Using vector beams in metrology applications, however, requires systems/techniques that can generate a wide variety of vector beams in a stable fashion. However, al-

though generation of vector beams has been studied since 1972 [13], such a source does not exist; the majority of the techniques used in the generation of vector beams employ interferometry and, as a result, generated vector beams suffer from phase instability [11, 12, 14]. Conversely, the handful of non-interferometric approaches [15, 16], while stable, are often limited by versatility. As a result, there is a clear need to develop a technique that can generate a wide variety of stable vector beams.

Although generating an optical field with the desired properties is an important step in optical metrology, delivering the generated optical field to the desired spatio-temporal location is of as much importance. This task is relatively less difficult when the positions of interest lie on the surface of the object being characterized. However, in metrology, oftentimes, the positions of interest lie inside or are obstructed by a highly scattering medium (HSM). For example, in deep tissue imaging, the interior regions of all samples are obstructed by the exterior regions which are scattering in nature. Similarly, in 3D integrated circuit (IC) metrology, characterizing components lying on the inner layers requires delivering light to those layers through the outer layers, and the outer layers act as strong scatterers due to the refractive index variations. In these situations, a way to control the state of the light transmitted through scattering media is necessary. Recently, there have been several studies related to this [17–24]. In 2007, it was shown that by iteratively changing the phase profile of the light incident onto a scattering sample light can be focused through it [17]. Later, it was suggested that measuring the transmission matrix of the scattering medium can lead to an increased versatility in controlling the transmission of light through scattering media [18]. Further, in 2011 [25, 26], it was shown that the randomness of a scattering medium can be used to control the temporal distribution of the pulses transmitted through it. These studies constitute important milestones in achieving the goal of delivering the light of desired properties through scattering media; however, many developments are required to get to that goal. Specifically, techniques to control the intensity, phase, and polarization of the light transmitted through such media are required as these are the properties that are most widely used in the metrology applications.

In this thesis, our focus is on addressing the aforementioned two needs. However, as a way of illustrating the power of polarization diversity in optical metrology, we also develop two optical metrology techniques that take advantage of vector beams. The first technique is a thin film characterization technique based

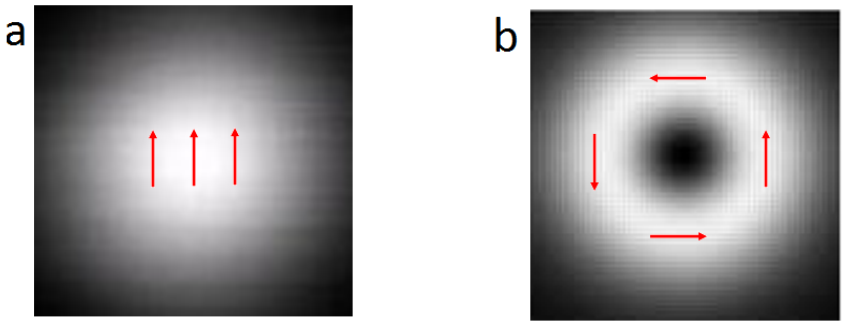

Figure 1.1: Beams with uniform (a) and non-uniform (b) polarization distributions. The local state of polarization is represented by the direction of the arrows.

on Mueller matrix polarimetry. The second technique is a technique to characterize the nonlinear optical properties of single nanoparticles. In the next section, we provide a very brief introduction to relevant concepts and prior work.

1.2 Background

1.2.1 Vector beams and vector fields

Most of the optical fields encountered in optics laboratories possess spatially uniform polarization distribution as shown in Fig. 1.1(a). However, of late, the optical fields with a (spatially) nonuniform polarization distributions, such as shown in Fig. 1.1(b) and known as vector fields [27], have garnered much attention [27, 28]. Vector beams are vector fields that are the beam-like solutions to the paraxial wave equations. These beams have been the subject of sustained research for the last several decades [13] as they have many interesting properties. For example, a radial beam, where the electric-field vectors align radially about the beam axis, results in a significant on-axis longitudinal electric-field component upon strong focusing [29]. An example focal field distribution for such a beam is shown in Fig. 1.2. Similarly, an azimuthal beam, where the electric-field vectors align azimuthally about the beam axis, results in a significant on-axis longitudinal magnetic-field component upon strong focusing. As a result of these exotic properties, vector beams have potential applications in a number of fields like high-resolution microscopy [29–32], surface chirality determination [33], real-time polarimetry [34], addressing and switching in magnetic cores memories [13], laser

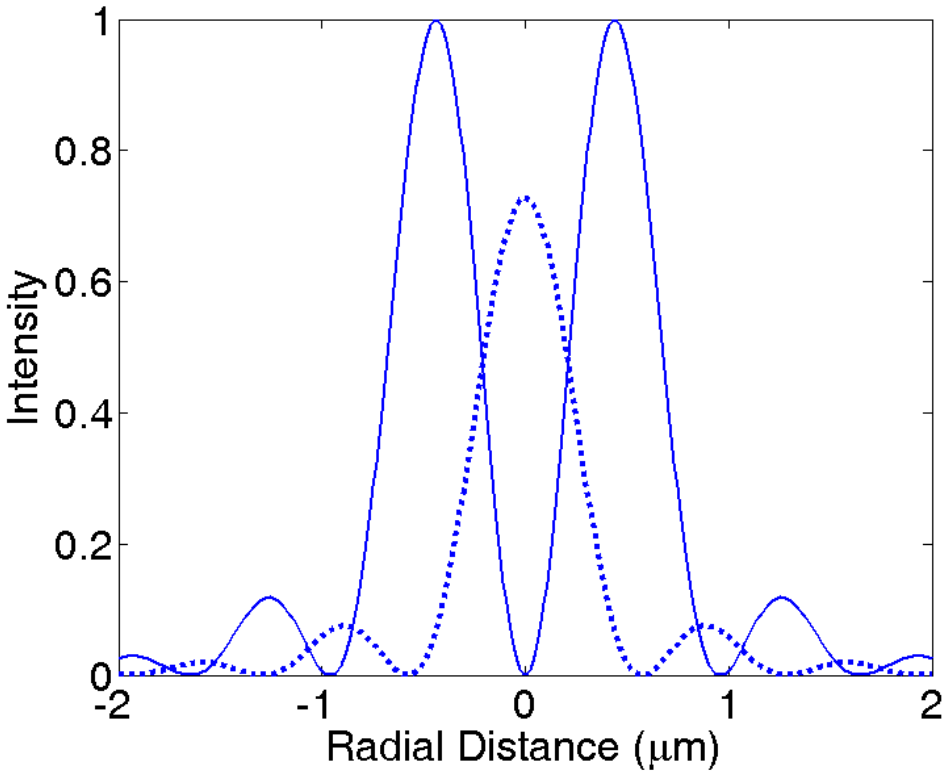

Figure 1.2: Transverse (solid line) and longitudinal (dashed line) components of the focal field distribution of a radially polarized beam as a function of the radial distance from the focal point.

machining [35], and light-matter interaction at the nanoscale [29, 36, 37] and have been studied for last several decades [13, 38]. Because of these potential applications, over the years, several techniques for generating vector beams have been reported [11–15, 38], which can be broadly classified as active and passive. Active techniques involve perturbing the laser cavity [38]; in contrast, passive techniques manipulate the optical field external to the cavity [12] to generate the vector beams. Compared to the active techniques, passive techniques are easier to implement and more widely used. Generating vector beams using the passive technique generally involves generating TEM_{01} and TEM_{10} modes and superposing them and is illustrated in Fig. 1.3. This process involves the use of which results in vector beams which are not stable. Using co-propagating beams to stabilize vector beam generation has been reported [11]. Similarly, non-interferometric approaches to generate each of the component beams have also been reported [15]. However, although stable, these techniques are severely limited in the types of

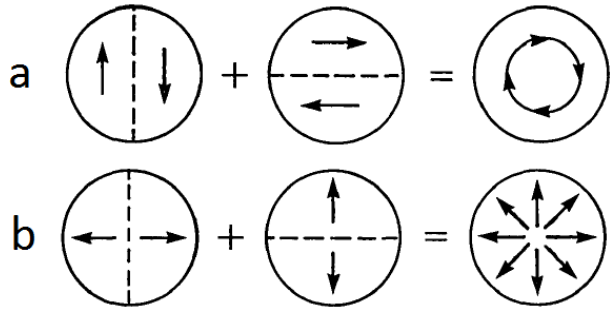

Figure 1.3: Illustration of the generation of the azimuthal (a) and radial (b) vector beams using superposition of TEM_{01} and TEM_{10} modes. Modified from [14].

vector beams they can generate.

1.2.2 Mueller matrix polarimetry

In recent years the demand for improved optical characterization techniques for material processing has increased due to, among other things, the continued miniaturization of components in the semiconductor industry, and the rapid development of a variety of nanostructured materials for photonic applications [39–44]. Precise characterization of such materials is necessary for process control, performance optimization, and device integration [45]. One approach to characterizing material optical properties is through the determination of its Mueller matrix, a mathematical description of material's linear optical properties including anisotropy and optical activity [45, 46]. To achieve this, Mueller matrix polarimetry (MMP) has been successfully invoked by way of a variety of experimental techniques [47, 48].

Figure 1.4 shows a generic polarimeter. As in any other polarimetry technique, determination of the elements of the Mueller matrix in MMP is typically done by analyzing the polarization of the light reflected from a sample as a function of the polarization of the incident light [48]. This involves two processes: polarization state generation (PSG), whereby the polarization of the incident light is varied systematically, and polarization state detection (PSD), in which the polarization of the reflected light is determined. Over the years a variety of optical components, such as rotating retardation plates [47–49], Pockels cells [50, 51], photoelastic modulators [52–54], and liquid crystal variable retarders [55, 56] have been used for PSG and PSD. Some common configurations in which these components have been arranged include rotating polarizer/rotating analyzer (RP/RA), rotating po-

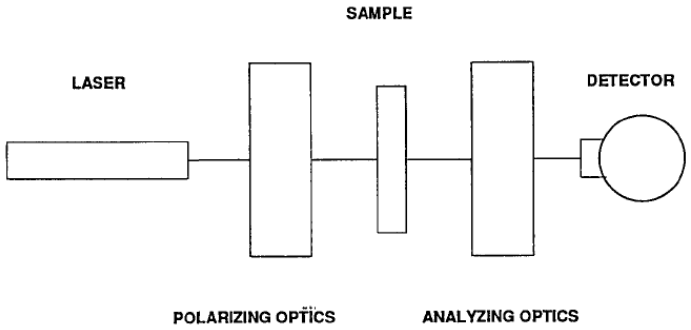

Figure 1.4: Schematic of a generic polarimeter. The polarizing optics is used to prepare the input states of polarization, whereas the analyzing optics and the detector are used to measure the state of polarization of the optical field transmitted through or reflected from the sample. Modified from [47].

larizer/rotating compensator fixed analyzer (RP/RCFA), phase modulator/phase modulator (PM/PM), dual phase modulator/dual phase modulator (DPM/DPM), and the like. However, irrespective of the optical elements used, or the particular configuration employed, all existing MMPs carry out the respective processes of PSG and PSD sequentially. For example, in the RP/RCFA configuration, the input polarization state is sequentially changed by way of a rotating polarizer, and likewise the reflected polarization state is analyzed sequentially via a rotating compensator (waveplate) followed by a fixed linear polarizer (analyzer) [48]. Similarly, in the DPM/DPM arrangement, the incident polarization is changed in time by changing the retardation of two variable retardation elements, and the reflected polarization is inferred by varying in time the retardation of two additional variable retardation devices [48, 52, 55].

Here, we note that, in MMP, the state of polarization is measured by using the Stokes vector. The Mueller matrix relates the optical field before and after an interaction through

$$\begin{bmatrix} S_0^{out} \\ S_1^{out} \\ S_2^{out} \\ S_3^{out} \end{bmatrix} = \begin{bmatrix} M_{11} & M_{12} & M_{13} & M_{14} \\ M_{21} & M_{22} & M_{23} & M_{24} \\ M_{31} & M_{32} & M_{33} & M_{34} \\ M_{41} & M_{42} & M_{43} & M_{44} \end{bmatrix} * \begin{bmatrix} S_0^{in} \\ S_1^{in} \\ S_2^{in} \\ S_3^{in} \end{bmatrix}, \tag{1.1}$$

where $\left[S_0^{in}, S_1^{in}, S_2^{in}, S_3^{in}\right]^T$ and $\left[S_0^{out}, S_1^{out}, S_2^{out}, S_3^{out}\right]^T$ are the Stokes vectors of the light before and after interaction, respectively, and T suggests matrix transposi-

tion.

1.2.3 Second-order susceptibility of nanoparticles

The polarization field in a medium that results from its interaction with an optical field is governed by its electrical susceptibility. At low optical intensities, the polarization field is predominantly governed by the linear susceptibility which is a second-rank tensor. However, as the intensity of the optical field is increased, the effect of second-order susceptibility becomes appreciable. The second-order nonlinear susceptibility which can be described by a tensor of third order, depends on the electronic configurations, molecular structures and alignments, and local morphologies of the system [57]. As a result, second harmonic generation (SHG) has been successfully used to investigate the local molecular alignment and/or the structure in a wide variety of materials including biological tissues [58], organic and inorganic crystals [59, 60], molecular materials, and surfaces and interfaces [61]. Recently, it has also been used to characterize individual nanoparticles [62–73]. In one study, the orientation and the crystalline nature of the individual organic nanocrystals were inferred from the SHG signal together with the two-photon excited fluorescence [63]. In another study, three-dimensional orientation of the individual nanocrystals was determined by imaging the emitted SHG signal using a defocused imaging system [62]. With biological samples it has been demonstrated that [74] the determination of the tensor elements provides additional information about the system. However, to-date, limited effort has been placed on determining the elements of the second-order nonlinear susceptibility tensor for individual nanoparticles.

Here, we note that not all elements of the third-rank tensor describing the second-order nonlinear susceptibility are independent of each other because of several kinds of symmetries, such as intrinsic permutation symmetry, overall permutation symmetry, spatial symmetry, and Kleinman symmetry. Under intrinsic permutation symmetry, the number of independent tensor elements is only 18. In this case, these elements of the third-rank tensor can be represented in a matrix form to relate the generated second-order polarization field to the incident optical

electric field through

$$\begin{bmatrix} \left(P^2_{2\omega}\right)_x \\ \left(P^2_{2\omega}\right)_y \\ \left(P^2_{2\omega}\right)_z \end{bmatrix} = \varepsilon \begin{bmatrix} d_{11} & d_{12} & d_{13} & d_{14} & d_{15} & d_{16} \\ d_{21} & d_{22} & d_{23} & d_{24} & d_{25} & d_{26} \\ d_{31} & d_{32} & d_{33} & d_{34} & d_{35} & d_{36} \end{bmatrix} * \begin{bmatrix} (E_\omega)^2_x \\ (E_\omega)^2_y \\ (E_\omega)^2_z \\ 2\,(E_\omega)_y\,(E_\omega)_z \\ 2\,(E_\omega)_x\,(E_\omega)_z \\ 2\,(E_\omega)_x\,(E_\omega)_y \end{bmatrix}, \qquad (1.2)$$

where ω is the fundamental frequency, $\left(P^2_{2\omega}\right)_i$ and $(E_\omega)_i$ are ith component of the polarization field and the incident field, respectively, whereas $i = x, y,$ and z. For those situations when the Kleinman symmetry is applicable, the number of independent parameters further decreases to 10.

1.2.4 Random media

Although known by many different names (random media [75], complex media [23], highly scattering media [20], disordered media [18]), material systems in which light undergoes multiple scattering events due to nanoscale refractive-index inhomogeneities are of much research interest because such materials are of technological and biological importance. There has always been an interest in controlling the transmission of waves through multiply scattering media. Such studies at the ultrasonic and microwave frequencies have been carried out for a long time [76]; however, it is only with the advent of spatial light modulators (SLMs) that similar studies have started to be carried out at optical frequencies.

One of the influential papers in this regard is by Vellekoop and Mosk [17] in which the authors focused light through a highly scattering sample which consisted of TiO_2. To focus the light, they iteratively changed the phase profile of the beam incident on the sample, taking the intensity of the light transmitted to a desired location as the feedback signal.

Later on it was shown that, in the presence of a source of feedback signal, light can also be focused inside a strongly scattering medium [77]. In the study, a fluorescent nanoscale probe was placed at the position of interest inside a strongly scattering medium. Focusing light to the desired location inside the sample was done by using the strength of the fluorescence signal as a feedback signal in optimizing the phase profile of the light incident upon the medium.

In these studies, the focus was on maximizing the strength of the light delivered to the desired spatial position. The effect of phase modulation on the total amount of light transmitted through the scattering samples was not measured. In a later study, it was shown that the total transmission of the light can also be increased by up to 44%.

Another milestone in these studies was the measurement of the transmission matrix in 2010 [18]. A transmission matrix gives the relation between the light that is incident upon the scattering sample and the light transmitted through it. Although the concept was introduced in [17], no attempt was made to measure it prior to 2010. In [18], Popoff et al. measured the transmission matrix by using phase-shifting interferometry. The measured transmission matrix was used to focus light through the scattering medium.

Since these influential papers, several interesting studies have been carried out in the field. Some of those include transmission of images through the scattering media [78], shaping of optical pulses [25, 26], and super-resolution focusing of an optical field [79]. One distinct line of investigation being carried out in the field is increasing the quality of control of the light transmitted through the scattering media, which has potential to be ultimately useful in optical metrology. In that aspect, we generalized the concept of transmission matrix to include the polarization property. We have also improved upon the experimental procedure for measuring the transmission matrix elements to be able to measure the absolute values of the transmission matrix elements.

1.3 Scope of the thesis

The focus of this thesis is to address the needs identified in Section 1.1. To that end, we have developed a novel technique to generate vector beams and vector fields. Our approach relies on the polarization rotation behavior of nematic liquid crystal spatial light modulators and a specially designed optical setup, and can generate a wide variety of vector beams and vector fields without using an interferometer. We have used the capability of the technique to generate a variety of vector fields and have studied their propagation properties. We discuss the generation technique and the propagation behavior of the vector fields in Chapter 2. As described in Section 1.1, the motivation behind developing a stable and versatile vector beam generator is the potential of harnessing the diversity of polarization

in metrology applications. In this thesis, we illustrate the usefulness of polarization diversity in optical metrology through two techniques. In one technique, known as rapid Mueller matrix polarimetry (RAMMP), we harness the diversity of polarization present in the vector beams to expedite the process of sample characterization. Specifically, we show that the vector beams in conjunction with an appropriately designed optical setup can be used to extract generalized ellipsometric parameters from a single image. This technique will be discussed in Chapter 3. In Chapter 4, we discuss a technique that has been designed to extract elements of the second-order nonlinear susceptibility tensor of single nanoparticle. This technique uses the diversity of polarization present in vector beams to improve the robustness of the measurement process. In Chapter 5, we present a low-cost phase-only SLM developed by using Texas Instruments' DLP LightCrafter DMD evaluation module. Although phase-only modulators have numerous applications, their use in optics laboratories is rather limited because of their high cost. The low-cost phase-only SLM presented here has potential to change that. We use the developed phase-only SLM to study the propagation of light through HSM. To that end, we have developed techniques to exercise quantitative control over the intensity and phase of the light that is transmitted through HSM. The novelties of our experimental design and experimental protocol in addition to our realization of the importance of a physical parameter hitherto overlooked in related studies are detailed in Chapter 5. In Chapter 6, we present our work on the controlling of the polarization of the light transmitted through HSM. To that end, at first, we introduce the concept of vector transmission matrix (VTM) that relates the transmitted field at an observation plane to the incident optical field in intensity, phase and polarization. We experimentally measured the VTM elements and used it to demonstrate the first-ever control over the polarization of the light transmitted through HSM. Our experimental results show that it is possible to use the randomness intrinsic to HSM as a polarization optic in order to control the polarization of the transmitted light. We discuss the theoretical, computational and experimental work that might help advance the field in Chapter 7 on future works.

CHAPTER 2

POLARIZATION CONTROL IN FREE SPACE: NON-INTERFEROMETRIC GENERATION OF VECTOR BEAMS AND VECTOR FIELDS

2.1 Introduction

In this chaper we present an approach to generating vector fields and vector beams that is stable and versatile. We use the approach to generate several example vector fields and study the basic propagation properties of some of them. The results presented in this chapter were published in [28].

2.2 Theory and experimental setup

To understand how we achieve versatile and stable vector-field generation, we begin by recalling a basic fact about nematic liquid crystal spatial light modulators (NLC-SLM). That is, the initial polarization state of an optical beam is altered by an NLC-SLM if the beam's initial polarization makes a projection on both the fast and slow axes of the NLC-SLM [80]. Thus, for a well-characterized NLC-SLM, this property can be exploited by the appropriate optical setup to effect the desired change in the polarization. In our scheme, the liquid crystal molecules of the NLC-SLM are aligned vertically with respect to the laboratory reference frame (the common reference henceforth used in this chapter). Changing the control voltage applied to each pixel of the NLC-SLM changes the path length traversed by the vertically polarized component of an input optical field, and thus the polarization at each point of the field corresponding to a particular pixel would change accordingly; the orthogonal component is not affected by the applied voltage.

Figure 2.1 illustrates the concept of vector field generation. We begin by restricting ourselves to using an input beam that is right circularly polarized (RCP); the effect of an input beam with arbitrary polarization will later be analyzed. For an RCP input beam, the output polarization state in the Jones vector representa-

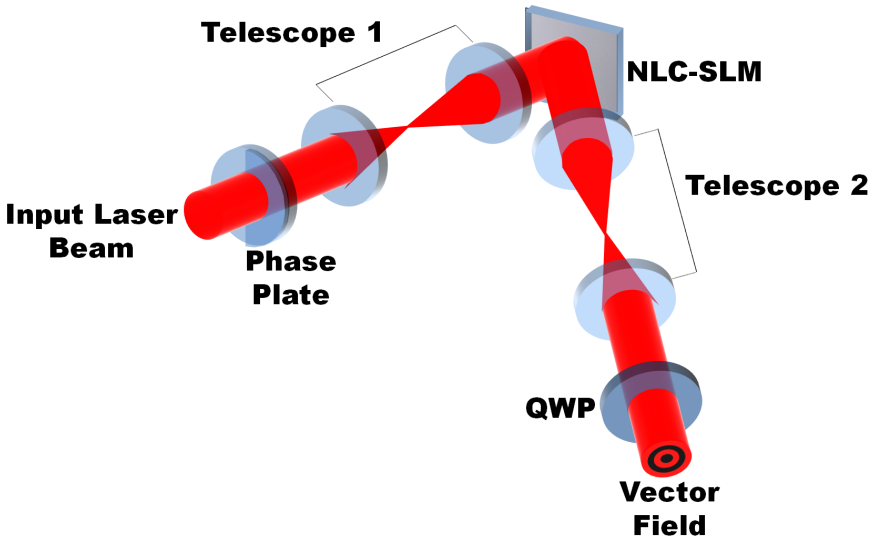

Figure 2.1: Illustration describing the concept of vector field generation. A right circularly polarized Gaussian beam is incident upon a phase plate. Telescope 1 images the phase plate onto the reflective NLC-SLM. Telescope 2 is then used to image the NLC-SLM surface onto the quarter-wave plate which has its fast axis aligned at 135° with respect to the horizontal axis. Light at the output of the quarter-wave plate is a vector field which can be converted to vector beams through spatial filtering or free space propagation. In our experiments, we use a Ti-Sapphire laser operating at 800 nm as the laser source. The phase plate, Lattice Electro Optics, 180° Phase-Half-UF-1006, consists of a 880-nm thick film of SiO_2 covering half of a glass window in order to impart a phase shift of 180° to half of the beam incident upon it. Our SLM is a 512×512-pixel reflective NLC-SLM (BNS XY Series Nematic SLM) and the quarter-wave plate is QWPO-800-06-4-R10 acquired from CVI Melles Griot.

tion [5], can be written as a 2×1 column vector $\begin{bmatrix} cos(\Phi/2) & sin(\Phi/2) \end{bmatrix}^{\top}$ [81], where Φ is the phase retardation imparted by the NLC-SLM, and the first and second elements of the vectors represent components of the field along the horizontal ($\hat{x}$) and vertical ($\hat{y}$) axes. This vector describes the output polarization at a point in the resultant field's cross-section. Note that using the Jones calculus to describe the polarization distribution across the field cross-section requires some care. First, unlike the standard case of an optical field with homogeneous (uniform) polarization distribution, the application of the Jones calculus to a field with inhomogeneous polarization requires that the Jones vector be modified to be a function of position. Second, the phase difference between different points in a field's cross-section must also be considered. With these constraints, the effect of the phase plate upon the beam can be represented as

$$J_{PP}(\varphi) = e^{i\pi sgn(\rho-\varphi)sng(\rho+\pi-\varphi)} \begin{pmatrix} 1 & 0 \\ 0 & 1 \end{pmatrix}, \tag{2.1}$$

where φ is the azimuth angle on the beam, and ρ is the angle the boundary of the phase transition on the phase plate makes with respect to $\hat{x}$. The term $sgn(\rho-\varphi)\,sgn(\rho+\pi-\varphi)$ ensures that the beam sees a phase step for azimuth angles between ρ and $\rho+\pi$ only. It should be noted that the phase term is a function of the position and cannot be discarded. To obtain a desired polarization distribution one has to carefully choose the spatial distribution of the retardation and the orientation of the phase plate. For a linear polarization distribution that possesses radial symmetry (such as in the case with radial and azimuthal vector beams), one can use a retardation value given by $(2\varphi+2\alpha)\,mod \quad 2\pi$, where α is the orientation of the polarization at $\varphi = 0$. Hence, the Jones vector of the field at the output of the quarter-wave plate (QWP) can be written as

$$J(\varphi) = e^{-i\pi\, sgn(\rho-\varphi)\, sgn(\rho+\pi-\varphi)} \begin{bmatrix} cos\left(\frac{(2\varphi+2\alpha)\ mod\ 2\pi}{2}\right) \\ sin\left(\frac{(2\varphi+2\alpha)\ mod\ 2\pi}{2}\right) \end{bmatrix}. \tag{2.2}$$

In this description, a polarization distribution identical to a radial beam can be obtained for $\alpha = 0$ and that for an azimuthal beam can be obtained for $\alpha = \frac{\pi}{2}$. This approach can describe any state of linear polarization. To generate polarization states possessing ellipticity the QWP in Fig. 2.1 can be removed. Under this condition, the Jones vector in Eq. (2.2) becomes complex

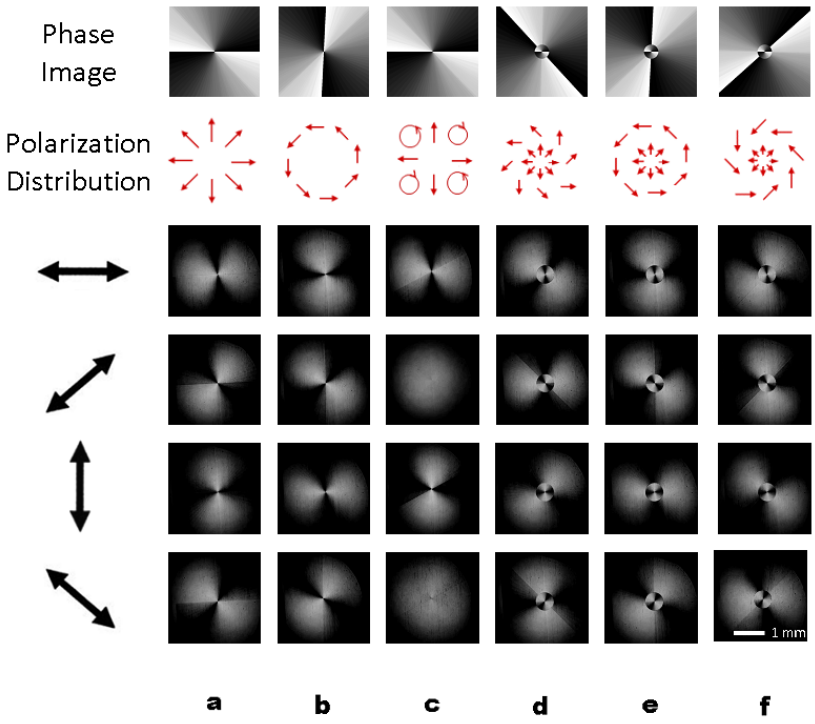

Figure 2.2: Experimentally obtained polarization analysis of the intensity distribution for single-mode (a-c) and hybrid (d-f) vector fields. Scale bar refers to 1 mm. The direction of the double-sided (black) arrows represent the direction of the transmission axis of the analyzer used.

$$J(\varphi) = e^{-i\pi\, sgn(\rho-\varphi)\, sgn(\rho+\pi-\varphi)} \begin{bmatrix} e^{\left(\frac{(2\varphi+2\alpha)\ mod\ 2\pi}{2}\right)} \\ ie^{\left(\frac{(2\varphi+2\alpha)\ mod\ 2\pi}{2}\right)} \end{bmatrix}. \tag{2.3}$$

The optical fields obtained at the output of the QWP are vector fields. Some of these fields can be converted to vector beams using spatial filtering or long distance propagation as shown in the next section.

2.3 Results and discussion

In Fig. 2.2 we show the versatility of our system by generating a variety of vector fields (shown in red). A polarization analyzer (Thorlabs, LPNIR050-MP), followed by a CCD camera (Watec, WAT-902H), is placed at the output of the QWP (the analyzer and CCD are not shown in the figure). Figures 2.2(a)-2.2(c) represents three single-mode fields, i.e., those possessing uniform radial symmetry

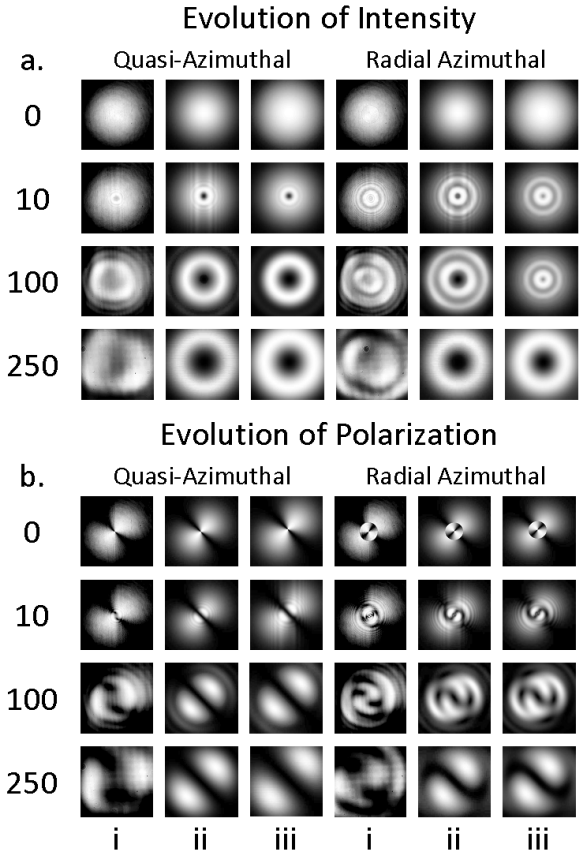

Figure 2.3: Evolution of the intensity, (a), and polarization, (b), for the quasi-azimuthal and radial-azimuthal vector fields, where the experimental (i) and simulation (ii and iii) data are shown for distances of 0, 10, 100, and 250 cm.

in polarization from the field center to the periphery, whereas Figs. 2.2(d)-2.2(f) represents three hybrid fields with radial distribution at the center (core). We observed that both the intensity and polarization distribution of the vector fields in Fig. 2.2 evolve with propagation, thus reiterating that the fields at the output of the QWP are not beam-like. Note that the QWP at the output is used to obtain all the states except for that shown in Fig. 2.2(c) which was obtained by removing the QWP and setting α to 0. The top row in the figure shows the respective phase image used for the generation of each vector field.

To understand the vector fields' propagation properties, we carried out numerical simulations using the angular spectrum representation [36, 37] as well as experiments. Specifically, we chose two types of fields: a single-mode field with an azimuthal polarization distribution, Fig. 2.2(b), which we call quasi-azimuthal, and a hybrid-mode field with a radial polarization distribution at the core and an

azimuthal polarization distribution at the periphery, Fig. 2.2(e), which we call radial-azimuthal. Both the total intensity and the projection through a 135° orientation of the analyzer (measured relative to horizontal axis) at propagation distances of 0, 10, 100, and 250 cm were recorded as shown in Figs. 2.3(a) and 2.3(b), column i. In column ii of Figs. 2.3(a) and 2.3(b), we show the corresponding simulations for both fields at these distances. To account for inevitable non-ideal step, for these simulations, we assume that the phase plate imparts both a phase and an amplitude error of $0.95e^{i\pi/6}$ in the vicinity of the phase step. In Figs. 2.3(a) and 2.3(b), column iii, we show results of the simulation assuming an ideal phase plate with no error. As can be seen from Fig. 2.3(a), upon propagation both the quasi-azimuthal and radial-azimuthal fields converge to a doughnut shape. The simulated values and the experimentally observed data are in good qualitative agreement. Further, we observe that the polarization distribution for both of these fields resembles that of the conventional azimuthal vector beam after propagation, with the accuracy of the approximation improving with increasing distance. This is confirmed in Fig. 2.4(a) for a simulation of the behavior of both field types for 30 m of propagation, where the left and right columns show the results for the quasi-azimuthal and radial-azimuthal fields, respectively. The top row shows the total intensity, and the bottom row shows the results of projection through an analyzer at 135°. The conversion to a beam-like solution after long distance propagation is interesting and results from the portion of the field that does not satisfy the beam-like property diffracting more strongly away from the optical axis compared to the portion of the field satisfying the beam like property. The fact that the radial-azimuthal field converts to an azimuthal beam upon propagation is also interesting. To appreciate the reason behind this we used the angular spectrum approach and found that the portion of this field near its geometric center has a larger divergence than the portion closer to the periphery which signifies that the center of the field is lost due to diffraction leaving behind a polarization distribution that resembles that of its peripheral region.

The conversion of the vector fields into conventional vector beams upon propagation is an interesting and important behavior. Most vector beam generation techniques employ the use of conventional spatial filtering to achieve beam-like solutions. Our approach provides an alternative. Figure 2.4(b) shows the effect of conventional spatial filtering on the quasi-radial beam. In the figure, columns i and ii represent the experimental and simulated results taking non-ideality of the phase plate into account, respectively. The top row in each case shows total in-

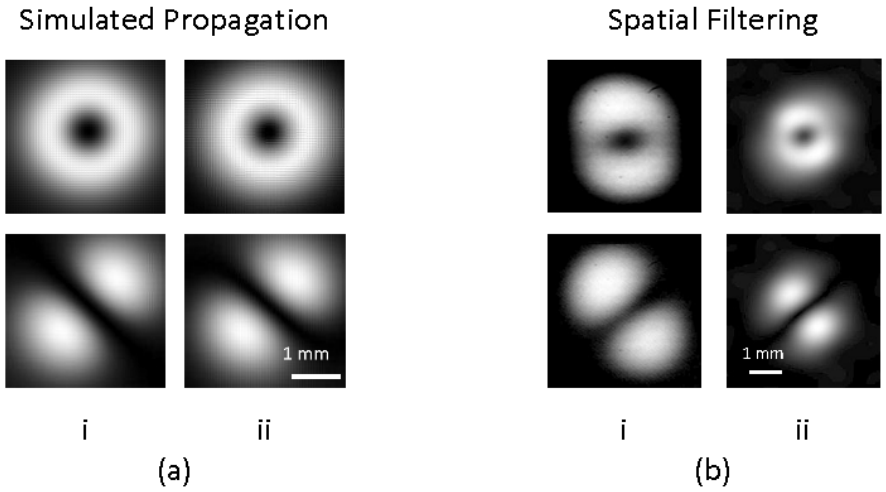

Figure 2.4: (a) Simulated propagation for 30 m is shown for quasi-azimuthal (i) and radial-azimuthal (ii) fields. (b) The effect of spatial filtering for the quasi-radial field, where (i) and (ii) show the experimental and simulated results, respectively. All scale bars are 1 mm.

tensity of the beam whereas the bottom row represents the projection of the beam through a 135° oriented analyzer. The experimental results are in good agreement with the simulations. It is expected that a phase plate with graded index profile will reduce the diffraction resulting from the phase step, thereby leading to better results. In general, the deviation from the ideal cases is due to both pixelation and the finite phase resolution of the NLC-SLM, but, as can be seen from Figs. 2.3 and 2.4(b), reasonable approximations can be experimentally achieved.

It has recently been shown that a HOPS representation could be used to describe vector beams [82]. We adapt this to describe those vector fields which possess polarization symmetries similar to that of the vector beams by noting that the representation used in [82] only specifies the polarization distribution and not the intensity distribution.

Next, we investigate the type of beams that can be generated by our setup. At first, we only consider an RCP input beam to the NLC-SLM. Expanding Eq. (2.2) and collecting similar terms for $sin(\alpha)$ and $cos(\alpha)$ we get $J(\varphi) = cos(\alpha) V_l + sin(\alpha) H_l$, where $V_l = cos(\varphi)\hat{x} + sin(\varphi)\hat{y}$, and $H_l = -sin(\varphi)\hat{x} + cos(\varphi)\hat{y}$ are the bases with topological charge $l = 1$, as shown in Eqs. (4) and (5) in [82]. In the orthonormal circular polarization basis [82] we can represent the above field as $J(\varphi) = [sin(\alpha) - i\,cos(\alpha)]/2R_l + [sin(\alpha) + i\,cos(\alpha)]/2L_l$, which, according to Eqs. (8)-(11) in [82], results in four Stokes vector elements of the form $S_0^1 =$

$1/2$, $S_1^1 = cos(\alpha)/2$, $S_2^1 = sin(\alpha)/2$, and $S_3^1 = 0$. These values relate to the coordinates for the azimuth angle $2\theta = tan^{-1}\left(S_2^1/S_1^1\right) = \alpha$ and the latitude angle $2\varphi = tan^{-1}\left(S_2^1/S_0^1\right) = 0$ on the HOPS. This indicates that for an RCP input to our system, the output states are limited to the equator of the HOPS. However, if the QWP in the output arm is removed, points outside the equator can be generated. This can be seen by starting with Eq. (2.3) and performing an analysis similar to the one followed for Eq. (2.2). Here, we add the caveat that Eqs. (12) and (13) in [82] use definitions of azimuth and latitude angles which are interchanged when compared to the generally used definitions in polarization optics [5].

The results described in this chapter have been for an RCP input beam. Now, we analyze the effect of an elliptically polarized input beam of the form $\hat{x} + i\,b\,\hat{y}$, where b is a complex coefficient relating to the weights of the orthogonal polarization components [83]. Such a beam can be generated by using a polarizer followed by an arbitrarily oriented QWP. Upon reflection from the NLC-SLM we obtain an output polarization proportional to $\left[e^{i\Phi} \quad i\,b\,e^{-i\Phi}\right]^\top$; this beam, when passed through a QWP with its fast axis at 135°, results in an output polarization proportional to $\left[e^{i\Phi} + b\,e^{-i\phi} \quad -i\,e^{i\phi} + i\,b\,e^{-i\Phi}\right]^\top$. For insight, we choose to rearrange this output polarization to the form $b\,R_l + L_l$, and observe that this resembles the equation of a general vector beam in a basis of right- and left-hand circular polarization, as shown in Eq. (1) in [82]. It has been shown that this equation represents any point on the HOPS with a topological charge of 1 [82], and thus we conclude that our setup can also generate all such states. It is worth highlighting that V_l and H_l are functions that describe the radial and an azimuthal vector beams, respectively. Since any state represented in the R_l and L_l basis can be represented in the V_l and H_l basis, all states on the HOPS result from a weighted superposition of radial and azimuthal vector fields.

2.4 Conclusion

In this chapter, we presented a non-interferometric technique to generate arbitrary vector fields and vector beams. Our approach is versatile and can generate any polarization distribution that corresponds to a coordinate on the higher-order Poincaré sphere, with basis functions of radial and azimuthal polarization. The stability resulting from our approach is expected to facilitate the use of vector beams in quantitative studies in metrology of anisotropic materials [34], mi-

croscopy [30], and nanophotonics [36]. As an illustrative example of the usefulness of the technique we analyzed the effect of propagation on some vector fields and interestingly found that, in general, these fields change polarization with propagation—a property of potential interest for systems requiring spatio-polarization-encoded activation for a specific reaction process such as in cross-linking of polarization sensitive polymers for three-dimensional fabrication. The experiments also showed that some vector fields convert to vector beams upon propagation which presents an alternative to the conventional spatial filtering in vector beam generation.

CHAPTER 3

APPLICATION OF POLARIZATION DIVERSITY IN THIN FILM CHARACTERIZATION: RAPID MUELLER MATRIX POLARIMETRY

3.1 Introduction

As pointed out in Chapter 1, existing Mueller matrix polarimeters need to collect time series data in order to characterize the sample. Here, we outline an approach that overcomes that shortcoming. Our approach relies on parallelizing the polarization state generation (PSG) and polarization state detection (PSD).

To parallelize the PSG process two requirements seem evident. First, it will be necessary to simultaneously deliver the required polarization diversity onto the samples; at least four linearly independent polarizations for complete Mueller matrix determination [48]. Second, it should be possible to uniquely relate each incident polarization to a corresponding reflected polarization. A practical solution that satisfies both constraints is to use vector beams because vector beams possess different states of polarization at different spatial points.

In Mueller matrix formalism, the polarization of light is represented by a four-element Stokes vector [84]. To parallelize the PSD, the individual Stokes vector elements of the reflected light need to be determined simultaneously. A straightforward approach to doing this might be to divide the reflected light into four beams. These beams could then be passed through separate optical setups designed to measure a different element of the Stokes vector. Though this approach based on amplitude division is conceptually straightforward, it would require multiples of optical elements potentially increasing unwanted error contributions from each element. Another approach might be to design an optical setup that modifies the polarization of the reflected light as a function of the position on the beam. Given a fixed analyzer and an array detector with such a setup, the intensity recorded at each point on the array detector would be a projection of the polarization along different polarization components. Thus, these intensity values, along with a priori knowledge of the optical setup, could be used to completely

determine the Stokes vector.

In this chapter, we present rapid Mueller matrix polarimetry (RAMMP) that achieves parallelization of both the PSG and PSD processes in real time and with high spatial resolution. We achieve parallelization of PSG by using vector beams, whereas to parallelize PSD a specially designed optical setup consisting of a microscope objective, an array detector, and an algorithm that combines information from different parts of the array detector is used. Our proposed scheme permits the extraction of twelve elements of the Mueller matrix from a single intensity image from the array detector, thereby reducing the experimental measurement time to the acquisition time of the array detector. To our knowledge the use of vector beams in polarimetry to improve polarization diversity on the sample has not previously been reported, thus our technique adds a new application domain. Moreover, use of a microscope objective provides diffraction-limited (spatial) sensitivity, which is very useful for the characterization of integrated circuits with ever decreasing feature size [85], and of nanostructures and nanomaterials that continue to become technologically and scientifically important [45]. The results presented in this chapter have been published in [34].

3.2 Theory

Figure 3.1 shows the proposed RAMMP optical setup. An input scalar polarized laser beam is converted into a collimated vector beam by the vector beam generator (VBG). The vector beam is then reflected by the beam splitter (BS) onto the microscope objective (OBJ). The focused beam first passes through the waveplate (WP) before being reflected by the sample, and subsequently re-collimated by OBJ after passing again through WP. Finally, the beam is analyzed by the fixed linear polarizer (LP) and imaged onto a CCD camera.

Typically, to calculate the electric field distribution on the sample one uses vector diffraction theory [86] and [37]. However, we are more interested in analyzing the polarization of the output beam as a function of the polarization of the input beam, and since both beams are collimated they can be treated as ensembles of rays [37]. Moreover, since we are interested only in the linear polarization properties of the sample, each ray in the output beam can be traced to a unique ray in the input beam. Therefore, we use a modified ray optics model in which each ray is associated not only with direction but also with intensity and polarization [37].

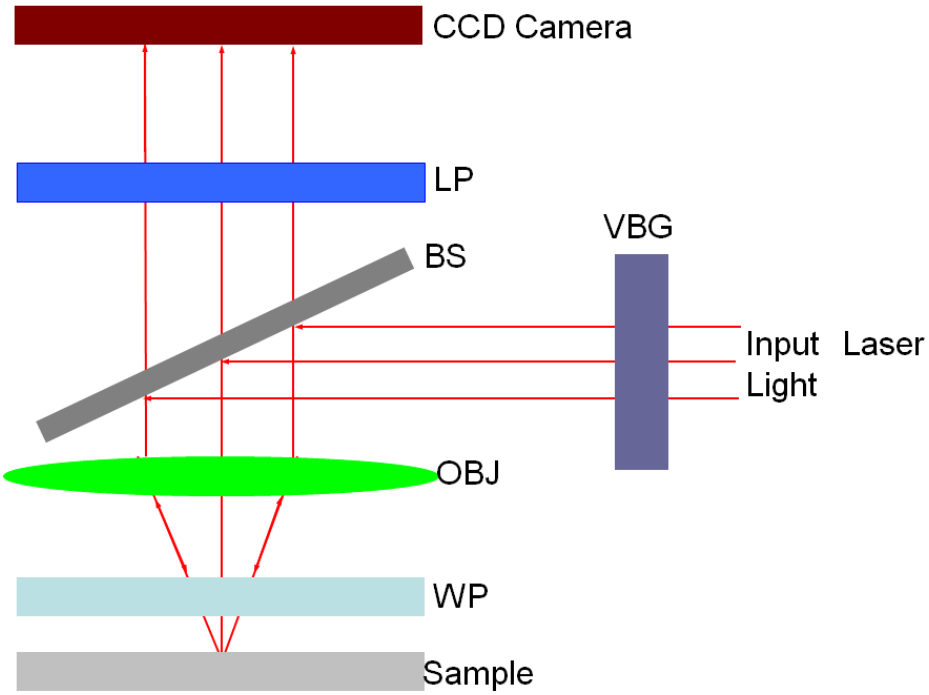

Figure 3.1: Schematic of the proposed experimental RAMMP setup. See text for details.

A Mueller matrix description of the setup is presented below.

To analyze the schematic shown in Fig. 3.1, we begin with the optical field on the back focal plane of OBJ. Let us consider a general incident ray located at radial distance r and azimuth angle Φ in the XOY coordinate system as shown in Fig. 3.2. Let its Stokes vector be

$$\boldsymbol{S}(r,\Phi) = [S_0(r,\Phi), S_1(r,\Phi), S_2(r,\Phi), S_3(r,\Phi)]^T, \tag{3.1}$$

where S_0, S_1, S_2, S_3 are the four elements of the Stokes vector, and superscript T represents the transpose of the row vector. Assigning polarization to a ray is for conceptual convenience, and is in accordance with the theory presented in [86] and [37]. Although the focusing action of OBJ on a ray can be represented in any coordinate system, it takes particularly simple form in a coordinate system which has its X axis lying on the plane of incidence of the ray. Because of this, for a ray at (r,Φ) we define a new coordinate system X_1OY_1 obtained by rotating the XOY coordinate system by an angle Φ counterclockwise. The Stokes vector in the new coordinate system X_1OY_1 is related to that in the old coordinate system

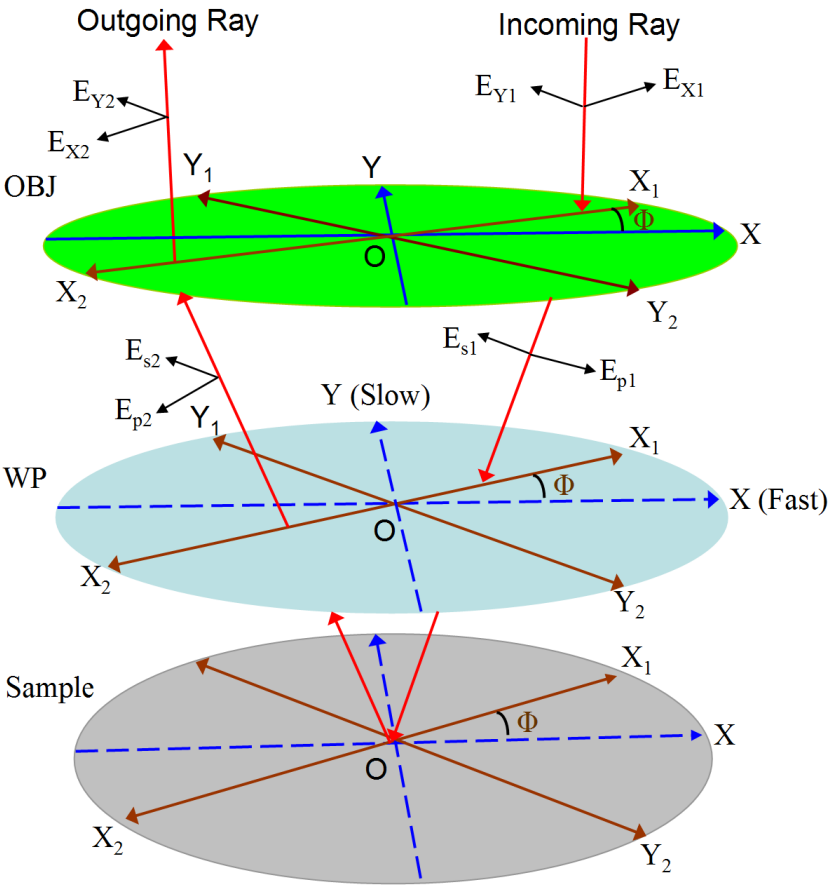

Figure 3.2: Schematic of the coordinate systems used in the derivation of the Mueller matrix description. The change in the polarization state of a general ray as it passes through the system is also shown.

XOY through a standard Muller matrix of the form [46]:

$$\boldsymbol{M}_R(-\Phi) = \begin{bmatrix} 1 & 0 & 0 & 0 \\ 0 & cos(2\Phi) & sin(2\Phi) & 0 \\ 0 & -sin(2\Phi) & cos(2\Phi) & 0 \\ 0 & 0 & 0 & 1 \end{bmatrix}. \tag{3.2}$$

In the rotated coordinate system upon refraction E_{x1} and E_{y1} transform to E_{p1} and E_{s1}, respectively (refer to Fig. 3.2). Due to this one-to-one transformation, the refraction operation of the lens can simply be written as,

$$\boldsymbol{M}_{RF} = \frac{1}{\sqrt{cos(\theta)}} \begin{bmatrix} 1 & 0 & 0 & 0 \\ 0 & 1 & 0 & 0 \\ 0 & 0 & 1 & 0 \\ 0 & 0 & 0 & 1 \end{bmatrix}, \tag{3.3}$$

where $\frac{1}{\sqrt{cos(\theta)}}$ follows from the intensity law of geometrical optics [37, 86]. Here θ is the cone angle of the ray and is defined as $tan^{-1}\left(\frac{r}{f}\right)$, where f is the focal length of OBJ [37, 86]. The refracted ray then passes through WP with its fast axis aligned along OX thereby making an angle of $-\Phi$ with OX_1 (refer to Fig. 3.2). The Mueller matrix of a waveplate with its fast axis at Φ and retardance δ is given by [46]

$$\boldsymbol{M}_{WP}(0,\delta) = \begin{bmatrix} 1 & 0 & 0 & 0 \\ 0 & 1 & 0 & 0 \\ 0 & 0 & cos(\delta) & sin(\delta) \\ 0 & 0 & -sin(\delta) & cos(\delta) \end{bmatrix}. \tag{3.4}$$

Thus, the effect of the waveplate on the ray, following standard Muller matrix transformation rules [46], is given by $\boldsymbol{M}_R(-\Phi)\boldsymbol{M}_{WP}(0,\delta)\boldsymbol{M}_R(\Phi)$. Generally, the retardance of a waveplate changes with the angle of incidence [87], and as such the setup has been designed to work for retardance values several degrees around that of a quarter waveplate. In general, the Muller matrix of any optical system is a function of both the angle of incidence and azimuth angle. The Mueller matrix for the sample at azimuth angle $\Phi = 0$ and cone angle of θ is, in general, given by

$$\boldsymbol{M}_S(\theta, \Phi = 0) = \begin{bmatrix} M_{11} & M_{12} & M_{13} & M_{14} \\ M_{21} & M_{22} & M_{23} & M_{24} \\ M_{31} & M_{32} & M_{33} & M_{34} \\ M_{41} & M_{42} & M_{43} & M_{44} \end{bmatrix}, \tag{3.5}$$

where $M_{11}, \cdots, M_{44}$ are Muller matrix elements. For a ray coming from (r, Φ), the sample appears to have been rotated by Φ, and thus the effect of the sample on the ray can be calculated by $\boldsymbol{M}_R(-\Phi)\boldsymbol{M}_{WP}(0, \Phi = 0)\boldsymbol{M}_R(\Phi)$. Reflection changes the direction of propagation of the ray and the polarization direction as shown in Fig. 3.2 (compare E_{s1} with E_{s2} and E_{p1} with E_{p2}). This change in polarization is represented by a Mueller matrix of the form:

$$\boldsymbol{M}_{RL} = \begin{bmatrix} 1 & 0 & 0 & 0 \\ 0 & 1 & 0 & 0 \\ 0 & 0 & -1 & 0 \\ 0 & 0 & 0 & -1 \end{bmatrix}. \tag{3.6}$$

This transformation, however, gives the Stokes vector in a new coordinate system, X_2OY_2 (refer to Fig. 3.2) which is related to X_1OY_1 through a clockwise rotation by π radians. For the reflected ray, the fast axis of WP makes an angle $(\pi - \Phi)$, and its effect on the ray therefore is given by $\boldsymbol{M}_R(\pi - \Phi)\boldsymbol{M}_{WP}(0, \delta)$ $\boldsymbol{M}_R(-\pi + \Phi)$. The collimation effect of the lens is modeled by the Mueller matrix

$$\boldsymbol{M}_{CL} = \sqrt{cos(\theta)} \begin{bmatrix} 1 & 0 & 0 & 0 \\ 0 & 1 & 0 & 0 \\ 0 & 0 & 1 & 0 \\ 0 & 0 & 0 & 1 \end{bmatrix}, \tag{3.7}$$

where $\sqrt{cos(\theta)}$ again follows from the intensity law [37]. The Stokes parameters obtained after all these transformations are in the X_2OY_2 coordinate system. To bring them back to our initial fixed coordinate system XOY, a counterclockwise rotation of the axes by $(\pi - \Phi)$ is required, i.e., $\boldsymbol{M}_R(-\pi + \Phi)$. The collimated ray then passes through LP with its transmission axis along OX and it transforms the Stokes vector according to [46]

$$\boldsymbol{M}_{LP} = \frac{1}{2}\begin{bmatrix} 1 & 1 & 0 & 0 \\ 1 & 1 & 0 & 0 \\ 0 & 0 & 0 & 0 \\ 0 & 0 & 0 & 0 \end{bmatrix}. \tag{3.8}$$

Finally, the intensity is recorded at the CCD. This operation is represented by

$$A = \begin{bmatrix} 1 & 0 & 0 & 0 \end{bmatrix}. \tag{3.9}$$

The combination of the aforementioned operations together gives the final expression for the intensity recorded at the CCD for a ray incident on OBJ at (r,Φ) or equivalently at (θ,Φ) to be

$$\begin{aligned} P(r,\Phi) =& \boldsymbol{A} * \boldsymbol{M}_{LP} * \boldsymbol{M}_R(-\pi+\Phi) * \boldsymbol{M}_{CL} * \boldsymbol{M}_R(-\pi+\Phi) \\ & * \boldsymbol{M}_{RL} * \boldsymbol{M}_R(-\Phi) * \boldsymbol{M}_S(\theta,\Phi=0) * \boldsymbol{M}_R(\Phi) * \boldsymbol{M}_R(-\Phi). \\ & * \boldsymbol{M}_{WP}(0,\delta) * \boldsymbol{M}_R(\Phi) * \boldsymbol{M}_{RF} * \boldsymbol{M}_R(-\Phi) * \boldsymbol{S}(r,\Phi) \end{aligned} \tag{3.10}$$

One observes that the output intensity is a function of the input Stokes vector, the azimuth angle, the radial distance (or the cone angle) and the elements of the sample Mueller matrix. By segregating the elements of the sample Mueller matrix, one can write the expression in the vector dot product form as

$$P(r,\Phi) = \overline{W} \cdot \overline{M} = \begin{bmatrix} W_{11} \\ W_{12} \\ W_{13} \\ W_{14} \\ W_{21} \\ \vdots \\ W_{44} \end{bmatrix} \cdot \begin{bmatrix} M_{11} \\ M_{12} \\ M_{13} \\ M_{14} \\ M_{21} \\ \vdots \\ M_{44} \end{bmatrix}, \tag{3.11}$$

where $\overline{W}$ and $\overline{M}$ are known as the polarimetric measurement vector and the Mueller vector, respectively [46]. This equation constitutes the forward model of the system. To determine the Muller matrix for a particular angle of incidence θ' i.e., $\boldsymbol{M}_S(\theta=\theta',\Phi=0)$, intensities on the array detector corresponding to that angle of incidence, i.e., intensities along a radial distance $r = f * tan(\theta')$ on the detector are arranged in the polarimetric data reduction equation [46] as

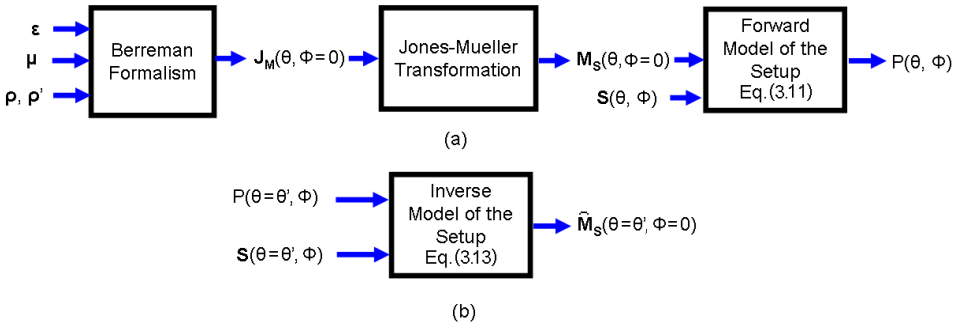

Figure 3.3: Systems block diagram representation of the steps taken for numerical analysis. Here (a) represents the approach for generating the synthetic data, and (b) the inverse model for retrieving the Mueller matrix elements of the sample.

$$\boldsymbol{P} = \boldsymbol{W}\overline{M} = \begin{bmatrix} P_1 \\ P_2 \\ \vdots \\ P_N \end{bmatrix} = \begin{bmatrix} W_{1,11} & W_{1,12} & \dots & W_{1,44} \\ W_{2,11} & W_{2,12} & \dots & W_{2,44} \\ \vdots & \vdots & \ddots & \vdots \\ W_{N,11} & W_{N,12} & \dots & W_{N,44} \end{bmatrix} \begin{bmatrix} M_{11} \\ M_{12} \\ \vdots \\ M_{44} \end{bmatrix}, \tag{3.12}$$

where N is the number of rays considered. Given $\boldsymbol{P}$ and $\boldsymbol{W}$, one can estimate $\overline{M}$ through [46]

$$\overline{\widehat{M}}_{Est} = \left(\boldsymbol{W}^T * \boldsymbol{W}\right)^{-1} \boldsymbol{W}^T \boldsymbol{P} = \boldsymbol{W}_P^{-1} \boldsymbol{P}, \tag{3.13}$$

where $\boldsymbol{W}_P^{-1}$ is the pseudoinverse of $\boldsymbol{W}$ and $\overline{\widehat{M}}_{Est}$ is the estimated Mueller vector. Estimated sample Mueller matrix $\widehat{\boldsymbol{M}}_S$ can be constructed from $\overline{\widehat{M}}_{Est}$ by using the relation implied in Eq. (3.11).

3.3 Results and discussion

To test the validity of RAMMP some straightforward numerical studies were carried out on two anisotropic samples, including a metamaterial. As shown in Fig. 3.3 numerical analysis involves two steps: generation of synthetic data which comprise the expected intensities at the array detector for a given sample, and the retrieval of the Mueller matrix elements from these intensities. To generate the synthetic data [as shown in Fig. 3.3(a)], values for the permeability ($\boldsymbol{\mu}$), permittivity ($\boldsymbol{\varepsilon}$), and rotation ($\boldsymbol{\rho}, \boldsymbol{\rho}'$) tensors [88] of the samples were obtained from the

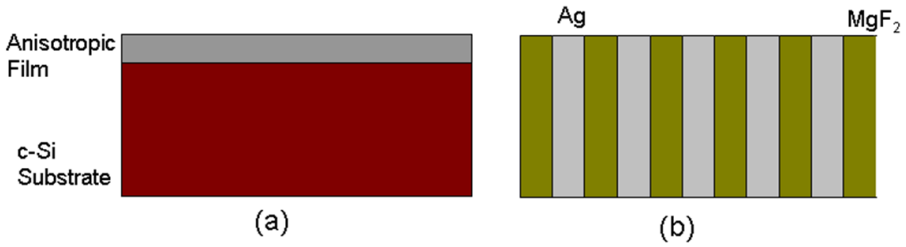

Figure 3.4: Schematic of samples numerically studied. (a) A thin anisotropic film deposited on top of a crystalline silicon sample. (b) Stratified metal-dielectric metamaterial.

literature. These values were then used to calculate the Jones matrix for reflection using the Berreman formalism, which is widely used to analyze the reflection and transmission of polarized light from stratified planar structures [88–90]. Furthermore, this formalism is particularly useful for analyzing arbitrary anisotropic samples irrespective of their orientation which is not possible using the Fresnel approach [90]. Since the Jones matrix for reflection for a given sample is a function of angle of incidence, and since in RAMMP the light is incident on the sample over a wide angular range due to the use of a microscope objective, an array of Jones matrices $[\boldsymbol{J}_M(\theta,\Phi=0)]$ for reflection were calculated. These Jones matrices were then converted to Mueller matrices $[\boldsymbol{M}_S(\theta,\Phi=0)]$ using the standard Jones-to-Mueller transformation [84]. Synthetic data $[P(\theta,\Phi)]$ was finally obtained by using the forward model of the system [Eq. (3.11)] in conjunction with the calculated Mueller matrices and field distribution of vector beams. At this stage of development, noise performance of the technique is secondary and we do not add noise to the synthetic data. To retrieve the Mueller matrix elements for angle of incidence θ', [$\widehat{\boldsymbol{M}}_S(\theta=\theta',\Phi=0)$ as shown in Fig. 3.3(b)] synthetic data corresponding to that angel of incidence were taken as a function of the azimuth angle Φ, and matrices $\boldsymbol{W}$ and $\boldsymbol{P}$ [defined in Eq. (3.12)] were constructed. The Mueller vector $\widehat{\boldsymbol{M}}_S$ was estimated using Eq. (3.13), and was constructed by rearranging its elements.

Schematics of the samples numerically studied are shown in Fig. 3.4. Figure 3.4(a) represents a thin film of a transparent uniaxial crystal deposited on top of a crystalline silicon substrate [90]. It is representative of materials like quartz and calcite which are widely used in optical components. The second sample depicted in Fig. 3.4(b) is a stratified metal-dielectric metamateial fabricated using Ag and MgF2 [91]. This material is magnetically active, i.e., the relative permittivity

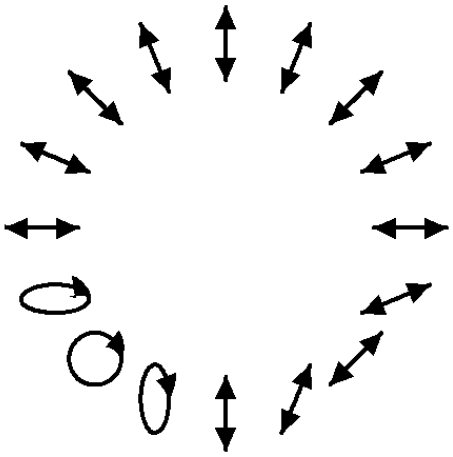

Figure 3.5: Polarization state distribution along the azimuth of the vector beam used in the calculations.

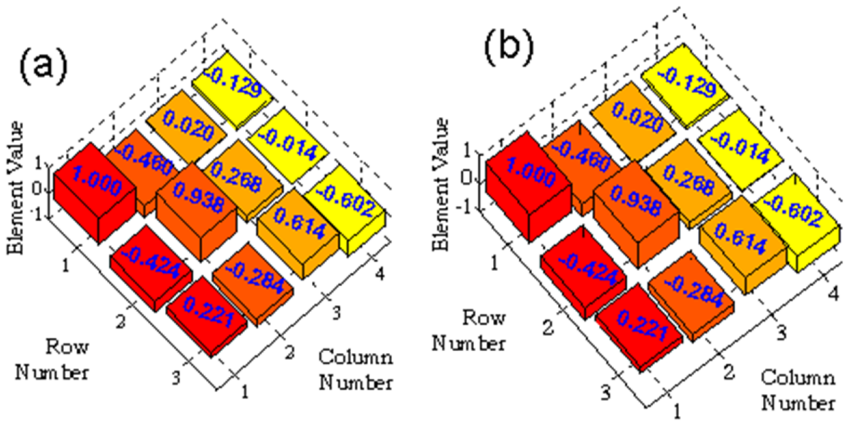

Figure 3.6: Mueller matrix elements for the sample in Fig. 3.4(a) as calculated from the (a) Berreman formalism, and as recovered using (b) RAMMP.

is not equal to 1, and is magnetically and electrically anisotropic. Iwanaga [91] shows negative (optical) refraction at a photon energy of 3.7 eV. This metamaterial structure has found its use, among other things, in the emerging hyperlens research [92, 93], which provides spatial resolution beyond the diffraction limit.

RAMMP uses vector beams to deliver polarization diversity on the sample. In our numerical studies we used a vector beam with polarization state distribution as shown in Fig. 3.5. Such a vector beam can be obtained from simply modifying the setups used to generate a radial vector beam to impart a relative phase shift of $\pi/2$ and π to the third and fourth quadrants of the constituent HG01 mode, respectively. Such a beam can easily be implemented by using spatial light modulators [12].

Figures 3.6 and 3.7 show a comparison between the Mueller matrix elements used to generate the synthetic data and the ones retrieved by solving the inverse problem as described earlier. The retrieved values are in exact correspondence with the original. Moreover, for each sample, only one intensity image is used to retrieve the Mueller matrix elements shown. This is made possible because of the parallelization of the PSG and PSD. Furthermore, RAMMP is flexible with the type of vector beam that can be used, as long as the input beam delivers four linearly independent polarization states on the sample simultaneously. However, to characterize isotropic samples, less exotic beams can be used.

Figures 3.6 and 3.7 show that RAMMP retrieves only twelve of the sixteen Mueller matrix elements, corresponding to the first three rows of the Mueller matrix. However, this is not a severe limitation. The elements from these three rows are sufficient to find all four complex elements of the Jones matrix of the sample within an absolute phase term [48]. Since a non-diagonal Jones matrix can accurately describe the polarization property of any type of non-depolarizing sample [88] including the emerging material structures that are magnetically active, this scheme is widely applicable. It is interesting to note that with a slight modification, RAMMP can allow determination of all the Mueller matrix elements. To do so, an additional intensity image needs to be taken by changing the orientation of the polarizer. Then, assuming that the polarizer is rotated by an angle ψ, $\boldsymbol{M}_{LP}$ in Eq. (3.10) will be replaced by $\boldsymbol{M}_R(\psi) * \boldsymbol{M}_{LP} * \boldsymbol{M}_R(-\psi)$. However, an alternative to collecting two images could be to modify the PSD such that all four elements of the Stokes vector could be retrieved from a single image as, in its current form, the RAAMP is limited to twelve elements because of the PSD that can extract only three elements of the Stokes vector from a single image.

The Mueller matrix of a general anisotropic sample is a function of both the azimuth angle and the angle of incidence. However, for a fixed angle of incidence one can relate the Mueller matrices at different azimuth angles by using Mueller matrix transformations for optical elements. This fact allowed us to take advantage of information overlap between intensities recorded for various azimuth angles for a fixed angle of incidence. However, the information overlap between intensities recorded for different angles of incidence is still unexploited. It is likely that combining this information will improve the robustness of the approach. This, however, is not possible within the framework of the Mueller matrix as no general relations exist to relate the Mueller matrices of different angles of incidence. An alternative approach might be to work directly with the optical matrix [88] that is

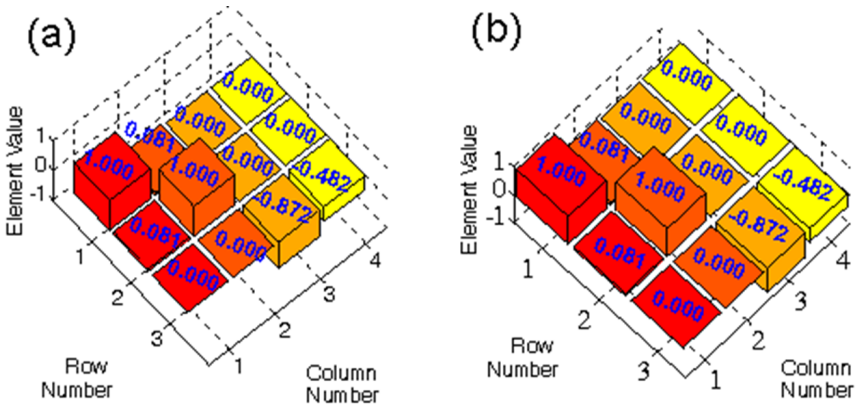

Figure 3.7: Mueller matrix elements for the sample in Fig. 3.4(b) as calculated from the (a) Berreman formalism, and as recovered using (b) RAMMP.

composed of the permittivity tensor, permeability tensor and rotation tensors.

3.4 Conclusion

In this chapter, we presented a rapid Mueller matrix polarimetry that can extract twelve Mueller matrix elements from a single intensity image. It achieves this by parallelizing the operation of the polarization state generator and polarization state detector, which is in stark contrast to the existing Mueller matrix polarimeters in which the respective polarization state generation and detection processes are done sequentially. Parallelization of the polarization state generation was achieved by using vector beams, for which our technique provides a new application domain. Polarization state detection was parallelized by using an array detector, a specially designed optical setup, and the realization that the Mueller matrices of optical elements with the same angle of incidence but different azimuth angles are related by standard Mueller matrix transformations. Numerical studies carried out on two anisotropic samples, one of which was a metamaterial, verified the approach. Future work includes experimental realization of RAMMP, and derivation of its description in the framework of the optical matrix [88] to make it a more information rich and robust characterization tool.

CHAPTER 4

APPLICATION OF POLARIZATION DIVERSITY IN NANOPARTICLE CHARACTERIZATION

4.1 Introduction

In Chapter 1, we pointed out the importance of measuring elements of the second-order nonlinear susceptibility tensor for individual nanoparticles. In this chapter, we present such a technique. Our technique utilizes a coherent confocal microscope [94], and exploits the fact that SHG is a coherent process so that the phase and the amplitude of the field may be obtained interferometrically [57, 61]. We assume that the particle is pointlike, that is, its structure is unresolvable on the scale of the wavelength of light [95] and that it can be characterized by a single second-order susceptibility tensor. Analysis of large particles may require a more complicated model [94]; however, the framework presented in this chapter is modular and is amenable to such modifications. We also assume that the particle is fixed in position and well isolated from other particles such that there is no inter-particle interaction, and that the optical field used to characterize the particle does not interact with neighboring particles. In a general setting, there is not enough data available to solve for all elements of the nonlinear susceptibility simultaneously. However, it is often possible to invoke symmetries of the tensor to reduce the number of free variables and resolve the remaining elements. The Kleinman symmetry [96, 97] may be invoked for nondispersive nonabsorbing media. Then the proposed technique can be used to infer the position and extract all elements of the second-order susceptibility. In the case of failure of the Kleinman symmetry, other symmetries may be invoked to similar ends [97]. Since in practice the overall scale of the data is not known precisely, the susceptibility tensor elements are estimated up to a constant scaling factor. For practical experiments, nanoparticles may be on substrates; the retrieved susceptibility in our approach is then the effective susceptibility that includes the effect of the substrate-particle interaction. The bare particle polarizability can then be inferred from the effective

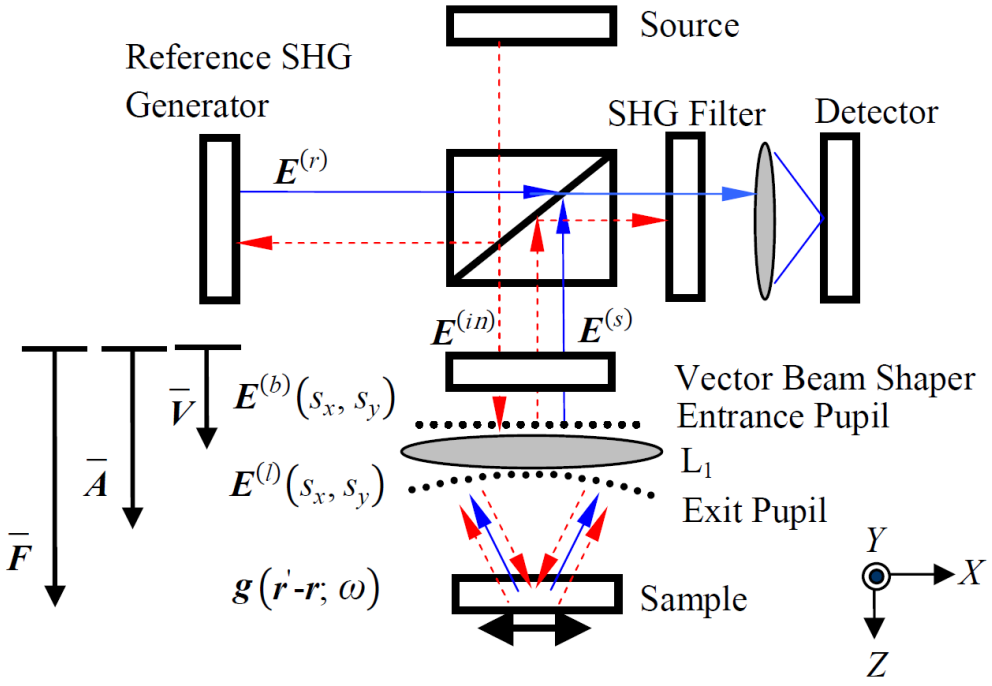

Figure 4.1: Schematic of the proposed experimental setup.

polarizability.

In Section 4.2 we describe the theoretical framework, and in Section 4.3 we present results from simulations. The results presented in this chapter were published in [36].

4.2 Theory

4.2.1 Forward model

Figure 4.1 shows a simplified schematic of the proposed experiment. An input beam with fundamental frequency ω (indicated in Fig. 4.1 by dashed arrows) passes through a beam splitter. Part of the beam passes through the vector beam shaper which imparts the required phase and intensity distribution to the input beam giving rise to a field $\boldsymbol{E}^{(b)}$ at the entrance pupil of the lens L_1. The beam is then refracted by L_1 which results in the field $\boldsymbol{E}^{(l)}$ at the exit pupil of the lens, and a field $\boldsymbol{g}$ in the focal volume. The sample consists of a substrate supporting the nanoparticle to be characterized. As mentioned in Section 4.1, the substrate can

have more than one nanoparticle; however, these nanoparticles should be sparsely distributed so that the focused beam interacts with only the nanoparticle to be characterized. The interaction of the nanoparticle with the focused optical field generates the backscattered signal $\boldsymbol{E}^{(s)}$ which consists of the optical field at both the fundamental and second harmonic (indicated in Fig. 4.1 by dotted arrows), 2ω, frequencies. This signal then propagates back through L_1 and is combined with a reference SHG signal, $\boldsymbol{E}^{(l)}(2\omega)$, at the beam splitter. The SHG filter in the signal path ensures that only the second-harmonic signal is recorded at the detector. The reference SHG signal can be generated using a nonlinear crystal with a large second-order susceptibility such as beta-barium borate (BBO) or lithium triborate (LBO) [57, 60, 61, 98]. It should also be noted that the reference SHG signal must be generated from the illuminating optical source in order to ensure that the reference field is coherent with the SHG signal backscattered from the nanoparticle (as demonstrated in [60]).

The intensity at the detector is a function of both the position of the geometrical focus $\boldsymbol{r} = (x, y, z)$, and the second-harmonic angular frequency 2ω, and can be written as [94, 99]

$$I(\boldsymbol{r};2\omega) = \left\langle \left| \boldsymbol{E}^{(r)}(2\omega) \right|^2 \right\rangle + 2\mathrm{Re}\left\{ S(\boldsymbol{r};2\omega) \right\} + \left\langle \left| \boldsymbol{E}^{(r)}(2\omega) \right|^2 \right\rangle, \tag{4.1}$$

where $\langle \cdots \rangle$ represents a time-averaging operation. In Eq. (4.1), the first term depends only on the reference signal; assuming a plane wave reference signal the dependence on r can be removed. The third term, which is the autocorrelation term, is typically very small and can usually be neglected [94]. The interferometric cross term defined as

$$S(\boldsymbol{r};2\omega) = \left\langle \left\{ \boldsymbol{E}^{(r)}(2\omega) \right\}^{\dagger} \boldsymbol{E}^{(s)}(\boldsymbol{r};2\omega) \right\rangle \tag{4.2}$$

can be recovered from its measured real part $\mathrm{Re}\{S(\boldsymbol{r};2\omega)\}$ using the Hilbert transform [94], where $\dagger$ represents the Hermitian transpose operator. Note that the application of the Hilbert transform in retrieving the complex field is applicable when the data is collected over a range of frequencies; alternatively, if the experiments are carried out at a single frequency, phase-shifting interferometry could be used. However, the fundamental results presented in this chapter are independent of the technique used to retrieve the complex field.

To determine the backscattered field, $\boldsymbol{E}^{(s)}(\boldsymbol{r};2\omega)$, we develop a forward model for the field from the incident field, through the optical system, to the interaction with the sample and back out. We denote the beam delivered by the source onto the vector beam shaper by $\boldsymbol{E}^{(in)}(\omega)$. It is converted to the field $\boldsymbol{E}^{(b)}(s_x,s_y;\omega)$ on the entrance pupil of the lens by the vector beam shaper where s_x and s_y are the components of the unit vector directed from a point on the exit pupil to the geometrical focus [37, 100] which can be mapped to a corresponding point on the entrance pupil by ray tracing, such that

$$\boldsymbol{E}^{(b)}(s_x,s_y;2\omega)=\vec{\boldsymbol{V}}(s_x,s_y)\,\boldsymbol{E}^{(in)}(\omega), \tag{4.3}$$

where $\vec{\boldsymbol{V}}(s_x,s_y)$ is a tensor operator describing the operation of the vector beam shaper. Assuming an aplanatic lens obeying the sine condition and the intensity law [37], the refracting action of the lens can be written as

$$\boldsymbol{E}^{(l)}(s_x,s_y;\omega)=\overline{A}(s_x,s_y)\,\boldsymbol{E}^{(in)}(\omega), \tag{4.4}$$

where the tensor $\overline{A}$ includes both the effect of the vector beam shaper and the refraction by the lens. This can be obtained from the rotation of Eq. (2.23) in [86] or from Eq. (3.51) in [37]. The field at an arbitrary point is calculated as [37, 94, 100]

$$\boldsymbol{g}\left(\boldsymbol{r}'-\boldsymbol{r};\omega\right)=\frac{k}{2\pi i}\int ds_x ds_y \frac{\overline{A}(s_x,s_y)\,\boldsymbol{E}^{in}(\omega)}{s_z(s_x,s_y)}e^{ik\boldsymbol{s}.(\boldsymbol{r}'-\boldsymbol{r})}=\overline{F}\left(\boldsymbol{r}'-\boldsymbol{r};\omega\right)\boldsymbol{E}^{in}(\omega), \tag{4.5}$$

where $\overline{F}$ is a tensor that includes the effect of the vector beam shaper and the lens. The parameter s_z , in free space, is related to s_x and s_y through the standard relation $s_z=\sqrt{1-s_x^2-s_y^2}$ [94]. The angular spectrum representation approach outlined here can also be modified to allow for situations where the field is focused onto a sample with background index mismatch [37].

Assuming that the nanoparticle is at a position $\boldsymbol{r}^p$ (p represents the position of the nanoparticle) and its effective 3×6 susceptibility tensor in contracted notation, i.e., the second-order susceptibility tensor under permutation symmetry, is represented by $\boldsymbol{d}$, the resultant second-harmonic polarization may be written as [96, 101]

$$P(2\omega) = \boldsymbol{d} \begin{bmatrix} {g_x}^2\left(\boldsymbol{r}^{(p)} - \boldsymbol{r};\omega\right) \\ {g_y}^2\left(\boldsymbol{r}^{(p)} - \boldsymbol{r};\omega\right) \\ {g_z}^2\left(\boldsymbol{r}^{(p)} - \boldsymbol{r};\omega\right) \\ 2{g_y}^2\left(\boldsymbol{r}^{(p)} - \boldsymbol{r};\omega\right) {g_z}^2\left(\boldsymbol{r}^{(p)} - \boldsymbol{r};\omega\right) \\ 2{g_x}^2\left(\boldsymbol{r}^{(p)} - \boldsymbol{r};\omega\right) {g_z}^2\left(\boldsymbol{r}^{(p)} - \boldsymbol{r};\omega\right) \\ 2{g_x}^2\left(\boldsymbol{r}^{(p)} - \boldsymbol{r};\omega\right) {g_y}^2\left(\boldsymbol{r}^{(p)} - \boldsymbol{r};\omega\right) \end{bmatrix} = \boldsymbol{d} \begin{bmatrix} e_1 \\ e_2 \\ e_3 \\ e_4 \\ e_5 \\ e_6 \end{bmatrix}, \tag{4.6}$$

where g_x, g_y and g_z are the x, y and z components of the focal field, g, and e_i is shorthand for the i th-row element of the 1×6 vector of products of the elements of g. The amplitude of the field resulting from this induced second-harmonic polarization is proportional to $k^2\boldsymbol{P}(2\omega)$ [99]. This field propagates back through the lens. By reciprocity, this operation can be described by $\overline{F}^T(2\omega)$ [94], where T refers to the transpose of the operator. Hence, the backscattered second-harmonic field can be written as

$$\boldsymbol{E}^{(s)}(\boldsymbol{r};2\omega)\,\alpha k^2 \overline{F}^T\left(\boldsymbol{r}^{(p)} - \boldsymbol{r}\right)\boldsymbol{P}(2\omega). \tag{4.7}$$

Note that $\overline{F}$ implicitly includes the dyadic Green's function which is frequency dependent [100, 102]. It should be noted that there is a backscattered fundamental field as well; however, it is neglected since it is filtered out. The backscattered field then interferes with the reference field. Using Eq. (4.2), the complex field can be written as

$$S(\boldsymbol{r};2\omega)\,\alpha k^2 \left\langle \left\{\boldsymbol{E}^{(r)}(2\omega)\right\}^{+} \overline{F}^T\left(\boldsymbol{r}^{(p)} - \boldsymbol{r};2\omega\right)\boldsymbol{P}(2\omega)\right\rangle. \tag{4.8}$$

Thus, one can acquire an image by fixing the focal plane at $z = 0$ and scanning the stage in two dimensions in (x,y). The received complex field, using the Einstein summation notation, can be written as

$$S(x,y;2\omega)\,\alpha d_{ij}(\omega)\,h_{ij}(x-x^p, y-y^p; z^p, 2\omega), \tag{4.9}$$

where h_{ij} are optical response functions (ORFs) which help discriminate the output signal due to each susceptibility element and are defined as

$$h_{ij}(x,y,z^p,2\omega) = k^2 {E^{(r)}}_l(2\omega)^* F_{il}\left(-x,-y,z^{(p)},2\omega\right)e_j. \tag{4.10}$$

In Eq. (4.9) the Einstein summation notation has again been used and * represents the complex conjugate. Also, the superscripts $i,l = 1,2,3$ and $j = 1,...,6$ represent corresponding elements of the parent tensor/vector. For example, F_{12} represents an element of the first row and second column of the operator $\overline{F}$. As Eq. (4.7) shows e_js are functions of the nanoparticle position. From Eq. (4.9), one sees that although the backscattered second-harmonic signal is a second-order function of the input field (through e_j), it is linearly dependent on the susceptibility elements. The ORFs defined in Eq. (4.10) are general. As noted above, it is not possible to solve for the elements of the susceptibility in the general case and so some prior constraint must be applied. Here we invoke the Kleinman symmetry as an example, which can be enforced when $\boldsymbol{d}$ is taken to have the following form [96]

$$\boldsymbol{d} = \begin{bmatrix} d_{11} & d_{12} & d_{13} & d_{14} & d_{15} & d_{16} \\ d_{16} & d_{22} & d_{23} & d_{24} & d_{14} & d_{12} \\ d_{15} & d_{23} & d_{33} & d_{23} & d_{13} & d_{14} \end{bmatrix}. \tag{4.11}$$

Equation (4.9) constitutes the forward model and can be used to predict the recorded signal when both the position $\boldsymbol{r}^{(p)}$ and the effective second-order susceptibility matrix $\boldsymbol{d}$ of the nanoparticle are known.

4.2.2 Inverse problem

To estimate the nanoparticle parameters, namely the susceptibility elements and the position of the particle, from the collected data, the inverse problem needs to be solved. This is achieved by searching for the set of parameters that lead to the smallest deviation between the observed data and that predicted from the forward model. There are several different quantitative metrics to estimate the deviation; here, we use the Euclidian norm

$$C\left(d, r^{(p)}; 2\omega\right) = \left\| S(\boldsymbol{\rho}; 2\omega) - d_{ij}(\omega)\, h_{ij}\left(x - x^{(p)}, y - y^{(p)}; z^{(p)}, 2\omega\right) \right\|. \tag{4.12}$$

The Euclidian norm chosen in Eq. (4.12) is consistent with a Gaussian noise model [103] characteristic of interferometer measurements dominated by the noise from the reference beam and/or thermal detector noise [104]. The information about the position and the susceptibility of the nanoparticle is encoded in the

recorded signal through the ORFs in Eq. (4.10), therefore successful retrieval of these parameters, as in any coding/decoding process, depends on the ability of ORFs to sufficiently encode each susceptibility element onto the recorded data. Specifically, the ORFs are required to each be distinct and non-negligible. Furthermore, since the ORFs are dependent on the input field in the focal region, successful use of this technique requires that an appropriate beam type be used. For example, the focal field for a Gaussian beam contains a negligibly small field of z polarization [37]. As a result, for the Gaussian beam, several ORFs, such as h_{13} are expected to be negligible as they depend on either the z or a product of the z- and the x- or the y-polarized field in the focal region. In contrast, a strongly focused radial vector beam, a beam with polarization distribution that is radially pointing outward from the beam center at each point [37], is also not expected to be a good choice for this technique because under very strong focusing a radial vector beam provides a strong z-polarized field at the expense of the x- and the y-polarized field [37]. In this case, ORFs such as h_{11} and h_{12} are expected to be negligible as they depend either on the x or the y, or a product of the z- with the x- or the y-polarized field. Here, we choose a modified radial beam that is focused using a 0.8 numerical-aperture lens. The vector beam generator used in our analysis blocks the central portion of the input beam and rotates the polarization at other points by an angle equal to the azimuthal angle of the point. Example techniques to generate such beams include the use of spiral phase delay plates, graded transmission filters [14], and spatial light modulators [12]. The resulting focal field distribution has comparable x- , y- , and z-polarization field strengths (see Fig. 4.2) which cannot be achieved by using a uniformly polarized Gaussian beam. Figure 4.3 shows the real and imaginary components of the first three of the ten independent spatial domain ORFs, using the modified radial beam, when the reference field is linearly polarized along the x-axis.

4.3 Simulations

To analyze the performance of the proposed technique numerical experiments were carried out. The nanoparticle parameters were generated randomly. One set of position values is shown in Eq. (4.13)

$$\boldsymbol{r}^{(p)} = \lambda_{SHG}\left[-0.0139 - 0.17774 - 0.0241\right]^T. \tag{4.13}$$

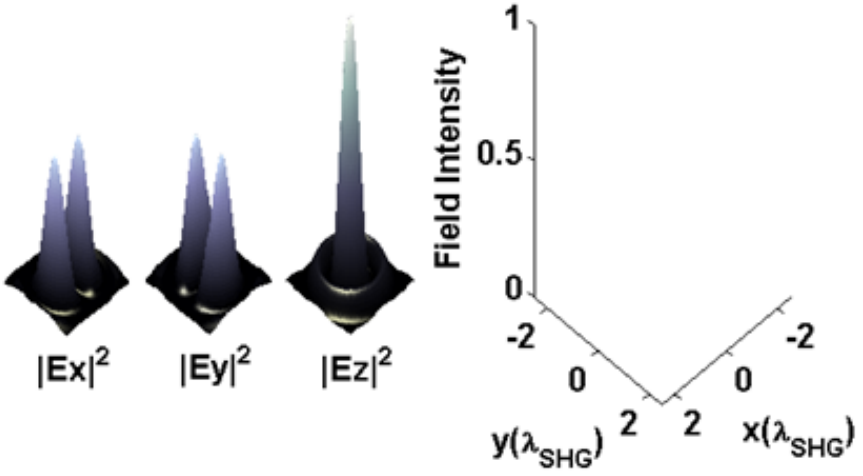

Figure 4.2: The intensity of each polarization component at the focal plane with the input beam and the lens parameters specified in the text. The intensities are normalized by the maximum intensity across all polarizations and all positions. The axes shown apply to all polarization components.

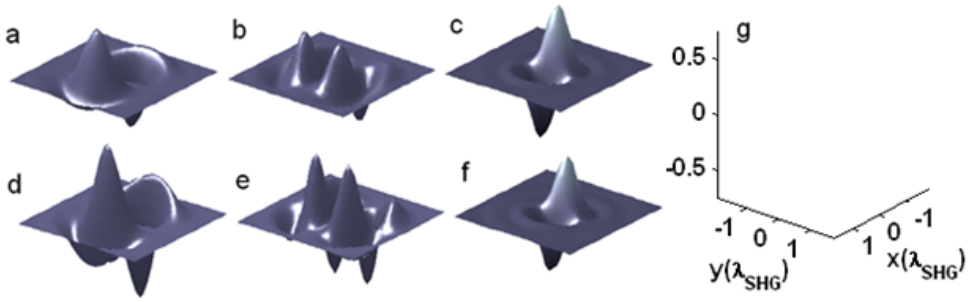

Figure 4.3: The real (a-c), and the imaginary (d-f) parts of the first three (of ten) spatial domain ORFs, h_{11}, h_{12} , h_{13} for a radial vector beam at a defocus of $0.125\lambda_{SHG}$ where $\lambda_{SHG} = 2\pi\frac{c}{2\omega}$. These ORFs are dependent on the input beam type as well as the amount of defocus, and encode the position and the susceptibility information of the nanoparticle onto the recorded signal. Thus, these ORFs can also be thought of as the basis elements, albeit non-orthogonal, onto which the measured field can be decomposed. The coefficients of the decomposition give us the ten independent elements of the second-order susceptibility tensor under the permutation and Kleinman symmetry. Figure 4.3(g) shows the scales used for these plots. Here, the axes have been labeled in the units of wavelength and the ORF values have been normalized by the maximum value across all ORFs. The axes shown apply to all ORFs.

The Kleinman symmetry assumes (optical) transparency [96], and as such the susceptibility elements should be real. An example of this is shown in Eq. (4.14) where the values have been normalized by the maximum value:

$$\boldsymbol{d} = \begin{bmatrix} 0.8274 & 0.5416 & 0.2956 & 0.0378 & 1.0000 & 0.7854 \\ 0.7854 & 0.6721 & 0.5913 & 0.7503 & 0.0378 & 0.5416 \\ 1.0000 & 0.7503 & 0.1569 & 0.5913 & 0.2956 & 0.0378 \end{bmatrix}. \tag{4.14}$$

The position $\boldsymbol{r}^{(p)}$ and the contracted susceptibility matrix $\boldsymbol{d}$ were then used in Eq. (4.9) to generate the synthetic data. It consisted of a 2D complex-field distribution $S(x,y;2\omega)$. In addition, since the data collected in actual experiments is never noise free, we choose to add complex random Gaussian noise. To generate an image with a given value of signal-to-noise ratio (SNR), for each pixel, the noise level is randomly chosen from a Gaussian distribution with the mean and variance defined by both the signal level at that pixel and the required SNR. Specifically, the real and the imaginary parts of the complex noise are generated independently from a Gaussian distribution whose variance is equal to half of the ratio of the signal power to the SNR. The power at each pixel is calculated as the square of the amplitude of the complex signal at that pixel.

To solve the inverse problem, the Nelder-Mead algorithm was applied over the particle position through the *fminsearch* function in MATLAB. The initialization point for the algorithm was randomly generated using the rand function in MATLAB with a range of 1.5 λ_{SHG} in the x- and y-directions centered on the origin. During each iteration, the corresponding elements of the susceptibility were calculated using matrix inversion of the data in Eq. (4.9). Without any restriction, *fminsearch* will converge to complex values. However, requiring the susceptibility to be real at the start of the optimization procedure derails convergence as this constraint introduces discontinuity in the objective function whereas *fminsearch* assumes continuous objective function. We circumvent this problem by permitting complex values at the beginning of the optimization procedure and restricting the susceptibility to be real once a minimum is approached.

For an SNR of 25 dB, the following values were estimated for position

$$\widehat{\boldsymbol{r}} = \lambda_{SHG}\,[-0.0141 - 0.1767 - 0.0239]^T \tag{4.15}$$

and susceptibility elements

$$\widehat{\boldsymbol{d}} = \begin{bmatrix} 0.8223 & 0.5325 & 0.2972 & 0.0342 & 1.0000 & 0.7813 \\ 0.7813 & 0.6690 & 0.5867 & 0.7451 & 0.0342 & 0.5325 \\ 1.0000 & 0.7451 & 0.1518 & 0.5967 & 0.2972 & 0.0342 \end{bmatrix}. \tag{4.16}$$

Again retrieved values have been normalized by the maximum real part. In practical systems the absolute scale of the data will not be known precisely hence the normalization is for comparison purposes so the susceptibility is estimated to within a constant scaling. We observe that the estimated value of the position closely matches the expected value [Eq. (4.13)] despite the noise. Also, comparing the elements of the matrix d with the elements of the matrix $\widehat{\boldsymbol{d}}$ we see that the values closely match despite the noise. It should be noted that in a physical experiment, the deduced susceptibility would be determined in the macroscopic (laboratory) reference frame. To correlate these values to the crystal structure, one will need to supplement retrieved values with knowledge of the orientation of the emission dipole (multipole) of the particle which can be obtained from techniques like defocused imaging [62].

The effect of the noise on the accuracy of the retrieved position and susceptibility is shown in Fig. 4.4. For each data point shown, numerical experiments were run ten times at a constant noise level and with a separate set of randomly generated nanoparticle parameters. The particle was restricted to the focal plane for all calculations. The error values shown are the average of the ten error values for each point. The confocal scanning step size in the transverse direction (along x- or y-) and in the axial direction was 0.125 λ_{SHG} and 0.25 λ_{SHG} , respectively. Figure 4.4(a) shows the norm of the error in the susceptibility elements. Similarly, Fig. 4.4(b) shows the Euclidian norm of the error in position $\widehat{\boldsymbol{r}}^{(p)} - \boldsymbol{r}^{(p)}$ as a function of the SNR. We observe the intuitive result that as the SNR is increased the error decreases. Since only 10 of the 18 elements are independent, to calculate the norm, a vector of these 10 elements was constructed and the corresponding Euclidian norm was calculated. It again shows an improvement in the retrieval accuracy as the noise level is decreased. Although in these calculations the particle is assumed to be in the focal plane (i.e., $z = 0$), our approach allows for the position and susceptibility of the particle to be retrieved even if the particle is located in any other plane.

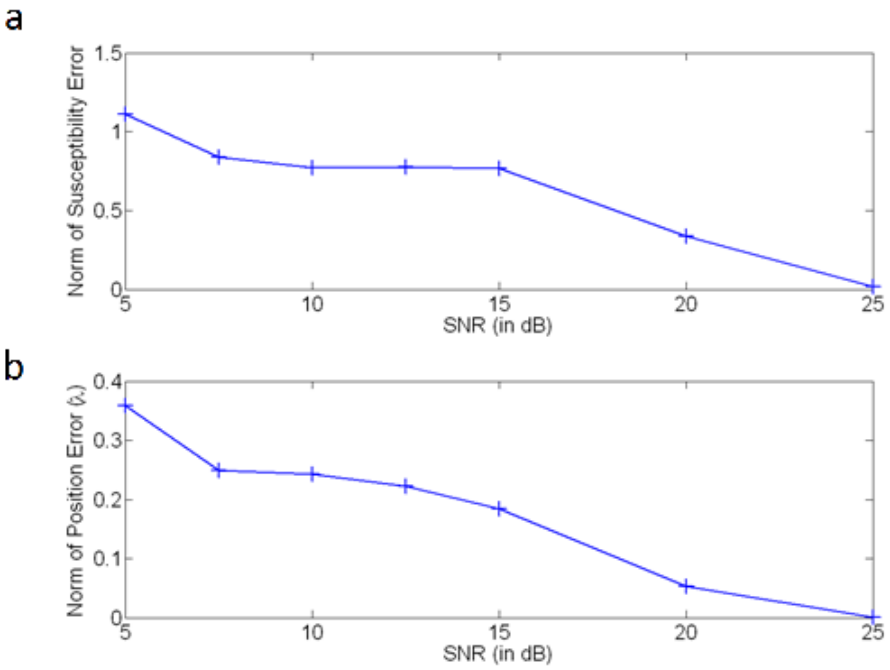

Figure 4.4: Euclidian norm of the error in the retrieved values of (a) the susceptibility, and (b) the position as a function of the signal-to-noise ratio.

4.4 Conclusion

We presented a technique to determine both the position and the second-order nonlinear susceptibility tensor elements for single nanoparticles under the permutation and Kleinman symmetry. The performance of the technique was assessed through the numerical experiments which showed that the retrieval is robust. Since the nanoparticles are placed on a substrate, the retrieved values of the susceptibility will be effective values in the sense that the effect of the substrate is also reflected in these values. This might be overcome by suspending the particle in a vacuum using optical levitation techniques. Furthermore, the framework presented in the preceding sections can be extended to extract information regarding third- and higher-order susceptibilities, as well as other types of coherent interaction processes. In the preceding sections we analyzed the case of non-absorptive nanoparticles. For absorptive particles the Kleinman symmetry condition is not applicable. Although the framework developed here can be used to analyze such particles, in that case not all elements of the susceptibility tensor can be unambiguously retrieved unless some other prior conditions which reduce the number of independent susceptibility tensor elements are applicable.

CHAPTER 5

QUANTITATIVE CONTROL OVER THE INTENSITY AND PHASE OF THE LIGHT TRANSMITTED THROUGH RANDOM MEDIA

5.1 Introduction

In this chapter, we demonstrate an ability to control both the amplitude and phase of the transmitted light after propagation through a random medium (RM). We show that the concept of the absolute value of the transmission matrix elements that we introduced in [20] can be used to design input beam profiles that can result in transmitted light of a desired intensity and phase. Although an approach for measuring the absolute value of the transmission matrix elements was presented by us in [20], the approach required that two separate beams, one for the reference signal and the other for the control signal, be used in the experiment, which limited the interferometric stability of the system. In the approach outlined in this chapter, by contrast, we encode both the reference and the control signals on a single beam. Further, we also find that the cross-correlation between different input channels, which has hitherto not been considered, plays an important role in the optimization process and needs to be taken into account.

This chapter is organized as follows. In Section 5.2, we discuss the measurement of the absolute value of the transmission matrix elements. In Section 5.3, we outline the approach used in the control of the intensity and the phase. This is followed by the results and discussion in Section 5.4. The chapter ends with the conclusions in Section 5.

5.2 Measurement of the transmission matrix elements

Figure 5.1 shows our experimental setup for measuring the transmission matrix elements. A collimated laser beam is incident on a deformable mirror device micromirror array (DMD-MMA) [105]. This DMD-MMA, acquired as part of the DLP

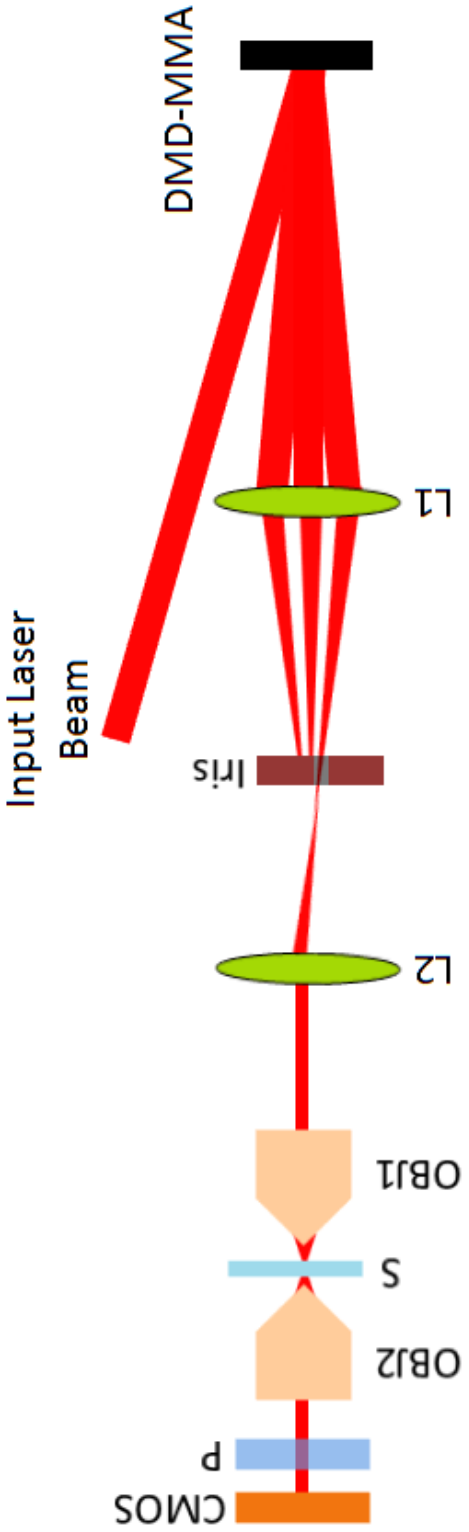

Figure 5.1: Schematic of the experimental setup.

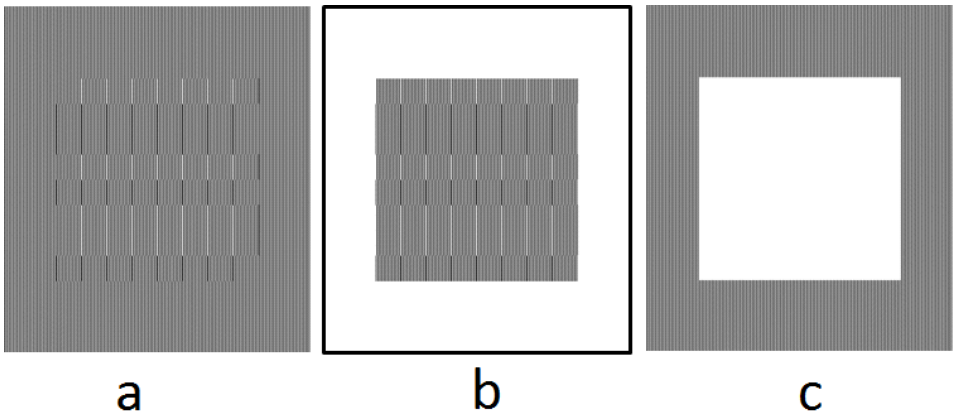

Figure 5.2: Hologram in (a) generates both the reference and control signal whereas those in (b) and (c) generate a control signal and the reference signal, respectively.

LightCrafter DMD evaluation module from Texas Instruments, can impart only a binary amplitude modulation to the field incident on it. However, measuring the transmission matrix elements requires an ability to perform a spatially dependent phase modulation [18–20]. We bridge this mismatch between the requirements of the experiment and the capability of the available device by using the Lee's synthetic binary holograms [106]. These holograms can be implemented through binary amplitude modulation and have been shown [19, 106] to be able to provide spatially dependent phase modulation. To achieve a phase-only modulation using the DMD-MMA, at first, from the desired phase profile $g(x,y)$, we calculate the Lee's synthetic binary hologram, $f(x,y)$, using the following expression [106]

$$f(x,y) = \begin{cases} 1 & \text{if } cos\left\{g(x,y) + \frac{2\pi x}{T}\right\} > cos(\pi q) \\ 0 & \text{Otherwise} \end{cases}, \tag{5.1}$$

where T is the period of the grating in the hologram. The parameter q defines the duty cycle of the grating [106] and is set to 0.5 in our case. Since the DMD-MMA is a pixelated device, we calculate the hologram function $f(x,y)$ only at the center of each of the available micro-mirrors. The calculated binary hologram is then displayed on the DMD-MMA which results in several diffraction orders. The desired phase modulation is in the first diffraction order, which is selected by obstructing the other orders at the Fourier plane of lens L1. The selected order is then collimated by lens L2. The desired phase modulation is observed at the front focal plane of the lens L2. This field is then focused onto the sample S by the objective OBJ1. Part of the scattered light is then collected by second objective

OBJ2 and passed through an analyzer P and recorded onto a CMOS camera. In our experiments, OBJ1 is an infinity corrected Spencer 10X objective of 0.25 NA, whereas OBJ2 is an infinity corrected Reichert 45X objective of 0.66 NA. Both the camera and polarizer used in our experiments were acquired from Thorlabs, with respective part numbers of DCC1545M and LPNIR100-MP. The scattering samples were prepared by depositing ZnO onto microscope slides. Here, we note that the DMD-MMA used in our experiments currently costs less than $600 which is significantly less expensive compared to the commercially available phase-only SLMs.

To measure the transmission matrix elements, we divide the DMD-MMA into two areas, the central control area and the peripheral reference area such that the measured matrix elements relate the input field corresponding to the control area to the field observed on the camera. The input field corresponding to the peripheral area provides the reference signal required in the four-point phase-shifting interferometry used in the measurement process. Figure 5.2 (a) shows an example hologram that extends over the whole DMD-MMA, whereas Figs. 5.2 (b) and (c) show holograms that cover only the control and reference areas, respectively. The control area is divided into 64 independently controllable control segments. Since the contribution of each control segment at the input to an observation point at the output is weak, measuring the transmission matrix elements in the canonical basis results in a low signal-to-noise ratio; therefore we measure the transmission matrix elements using a Hadamard basis at the input [18, 20]. The measured transmission matrix elements are of the form

$$t_{n,m} = |g_{nm}| \sqrt{I^C_{n,m} I^R_{n,m}} e^{i\varphi_{n,m}}, \tag{5.2}$$

where $I^C_{n,m}$ and $I^R_{n,m}$ are the intensities of the control and reference signals at the nth observation point corresponding to the mth Hadamard basis element input. Similarly, $\varphi_{n,m}$ is the phase difference between the control and reference signals. The cross-correlation term $|g_{nm}|$ defines the correlation between the reference signal and the control signal at the nth observation point corresponding to the mth Hadamard basis element input. In the previous studies [18, 20], this term has been overlooked. However, we find its inclusion to be crucial in exercising a quantitative control over the intensity and phase of the transmitted light.

Ideally, the transmission matrix elements should not depend upon the reference signal used in their measurement. However, Eq. (5.2) shows that the measured

transmission matrix elements depend upon the reference signal in addition to the control signal. To filter out the effect of the reference signal, we measure the strength of the reference signal at each of the observation points. To measure the strength of the reference signal, we turn off the control area on the DMD-MMA by displaying the hologram of Fig. 5.2 (c) on the DMD-MMA. Then we measure the intensity of the transmitted optical field which gives us the strength of the reference signal. This allows us to measure the absolute values of the transmission matrix elements of the form

$$t_{n,m} = |g_{nm}| \sqrt{I^C_{n,m}} e^{i\varphi_{n,m}}, \tag{5.3}$$

which does not depend upon the reference signal.

In our experiments, we also calculate the amplitude of the cross-correlation term. To do that, we measure the strength of the control signal by turning off the reference area on the DMD-MMA, and then measuring the strength of the transmitted field. To turn off the reference area on the DMD-MMA, we display the hologram of the form Fig. 5.2 (b) on the DMD-MMA. Once the strength of the control signal has been measured, $|g_{nm}|$ is calculated as

$$|g_{nm}| = |t_{n,m}| \,/\, \sqrt{I^C_{n,m}}. \tag{5.4}$$

In our experiments, we found that calculating $\varphi_{n,m}$ and $|g_{nm}|$ and hence the $t_{n,m}$ through curve fitting consistently provides better results. To measure these parameters through curve fitting, the intensity at the nth observation point corresponding to the mth Hadamard basis element phase modulated by α is described by

$$I_{n,m} = I^C_{n,m} + I^R_{n,m} + 2\sqrt{I^C_{n,m} I^R_{n,m}}\, |g_{nm}|\, cos\left(\varphi_{n,m} + \alpha\right), \tag{5.5}$$

and the curve fitting is done with $|g_{nm}|$ and $\varphi_{n,m}$ as the free parameters. α and $I_{n,m}$ are the independent and dependent variables, respectively, whereas $I^C_{n,m}$ and $I^R_{n,m}$ are the problem dependnet parameters. $I_{n,m}$ is measured corresponding to $\alpha = 0, \pi/2, \pi,$ and $3\pi/2$ as part of the phase-shifting interferometry, and $I^C_{n,m}$ and $I^R_{n,m}$ are measured as described above. Although the transmission matrix elements are measured in Hadamard basis input, we convert them to canonical basis input $T_{n,m}$ using standard Hadamard to canonical conversion [107] before using them in the further optimization processes.

5.3 Controlling the intensity and phase

To control the intensity and/or phase of the transmitted light using the transmission matrix, one needs to design and implement an input field profile that would result in the desired transmitted field. In our experiments, we design the desired input fields using the computational optimization techniques. For example, an input phase profile that would result in a desired intensity I_n^D at a chosen observation point n is calculated by solving the optimization problem of the following form:

$$\underset{\phi_m}{\text{Minimize}} \left(\left| u_n^P \right|^2 - I_n^D \right)^2, \tag{5.6}$$

where ϕ_m is the phase modulation to be applied to the mth control segment. The predicted value of the field u_n^P needed in the optimization process is calculated as

$$u_n^P = \sum_m T_{n,m} e^{i\phi_m}. \tag{5.7}$$

Once a phase profile is designed, corresponding holograms are generated using Eq. (5.1) and then displayed on the DMD-MMA. Here we note that, in Eq. (5.7), it is assumed that the magnitude of the cross-correlation between different components is 1.

To deliver an optical field of intensity I_n^D at a phase of ϕ_n^D, one needs to solve the optimization problem of the following form:

$$\underset{\phi_m}{\text{Minimize}} \left(\left| u_n^P \right|^2 - I_n^D \right)^2 \text{ subject to } \angle u_n^P = \phi_n^D. \tag{5.8}$$

This basic idea described above can be extended to multiple points or an entire region.

5.4 Results and discussion

At first, we discuss our results on the quantitative control of the intensity of the light transmitted through a highly scattering medium (HSM). The results are shown in Fig. 5.3. To collect these results, we, at first, measured the transmission matrix elements. Then we selected the regions to be studied. These regions were randomly selected under the constraint that at least 50 of the 64 transmission matrix elements of the selected region had measured $|g_{nm}|$s between 0.7 and 1. For each selected region, we calculated 25 phase profiles, each predicted to generate

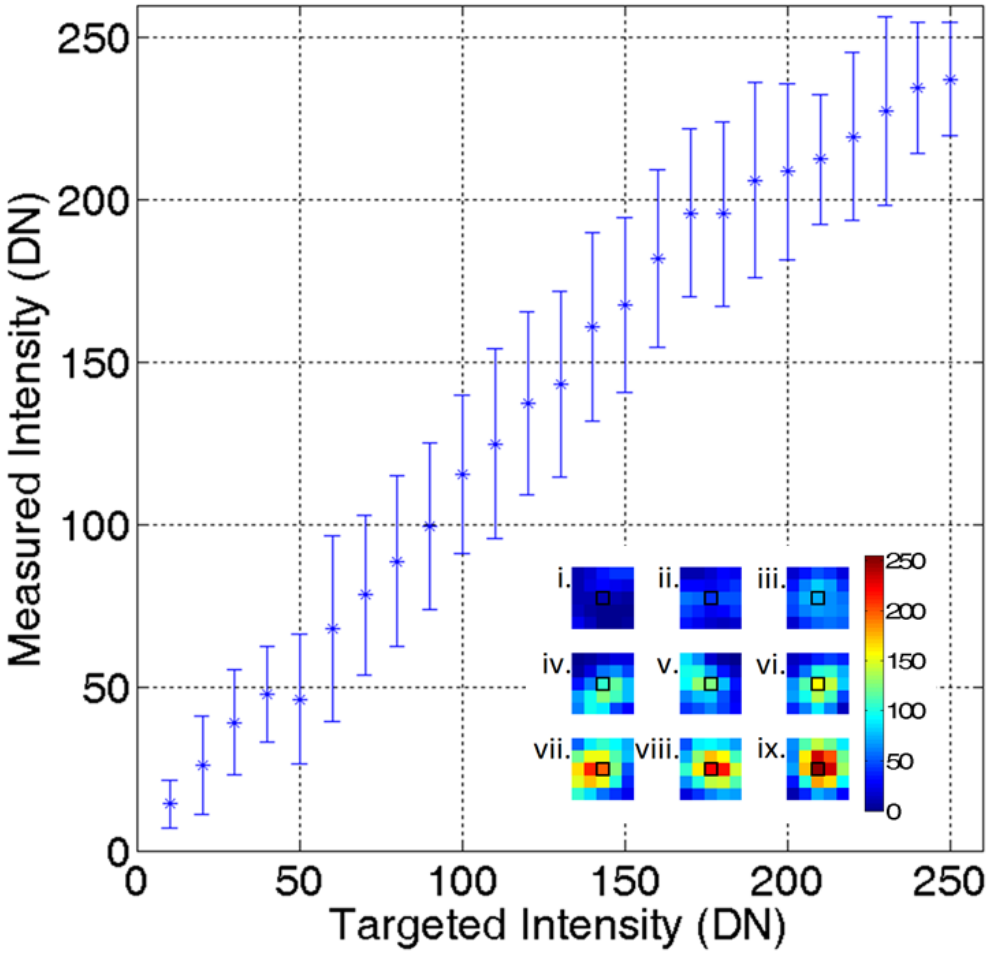

Figure 5.3: Experimentally observed intensities versus the targeted intensities. Inset shows example intensity distribution at and around the area at which the intensity was controlled. The targeted area is shown by a black square. The intensity distributions are shown for the targeted intensities of 10, 40, $\cdots$, 250 in images i, ii, $\cdots$, ix, respectively.

one of the 25 targeted intensities at that region. Then we generated input optical fields with the prescribed phase profiles using the binary holograms calculated according to Eq. (5.1). Finally, we measured the respective transmitted intensities at the region of interest and compared the measured intensities with the targeted ones. From the figure, we see that the measured values follow the targeted ones with a maximum standard deviation of less than 20 DN. These results are first of their kind showing the use of the transmission matrix in delivering the light of the desired intensity at the desired location through an HSM.

This level of control over the transmitted intensity throughout the observation plane should be possible by changing the model of the system used in the process of calculating the phase profile. Currently, we assume a completely coherent interference in calculating the phase profile. We minimize the violation of this assumption by restricting our attention to the regions in the observation plane where $|g_{nm}|$ values are large. This shortcoming can be removed by assuming that each control segment contributes a partially coherent field to the region of interest and predicting the intensity at the region of interest as

$$I_n^P = \sum_m |T_{n,m}|^2 + \sum_m \sum_{m',m' \neq m} \left| g_{m,m'}^n \right| \sqrt{|T_{n,m}|^2 \left| T_{n,m'} \right|^2} cos(\delta_{m,m'}^n), \tag{5.9}$$

which governs the interference between multiple partially coherent waves. Here, $\left| g_{m,m'}^n \right|$ is the magnitude of the cross-correlation between the contributions of the mth and m'th control segment to the nth observation point, whereas $\delta_{m,m'}^n$ is the phase difference between those contributions. To use this expression in the experiments, $\left| g_{m,m'}^n \right|$s will have to be measured. One approach to measuring these values would be to perform pairwise interference meaurements between the contributions of all the available control segments. However, one problem with this approach could be a low signal-to-noise ratio. An alternative approach that would not suffer from a low signal-to-noise ratio would be to measure the transmitted intensities corresponding to at least ${}_MC_2$ distinct input phase profiles and to solve the resulting system of linear equations. Here, M refers to the number of control segments used in the experiment.

Figure 5.4 shows our experimental results on the controlling of the phase of the light transmitted through an HSM. In this case also, we restricted ourselves to the regions on the observation plane that had at least 50 of the 64 measured $|g_{nm}|$s larger than 0.7. For each selected region of interest, we calculated input

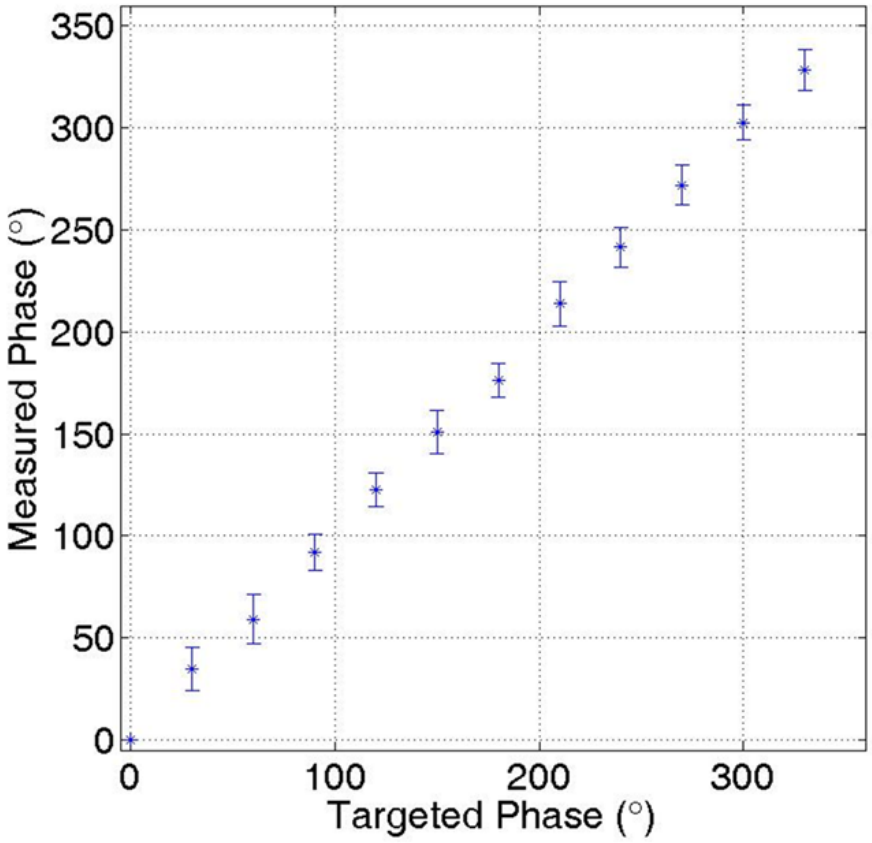

Figure 5.4: Experimentally observed phase values versus the targeted phase values for a constant targeted intensity of 190 DN.

Figure 5.5: Quantitative control of intensity at multiple points: in (a) we optimize for the right region to be brighter whereas in (b) left area is tuned to be brighter.

phase profiles to generate a constant targeted intensity of 190 DN and a range of phase values going from 0 to 330° at an interval of 30° using the approach outlined in Section 5.3. From the calculated phase profiles we calculated four phase profiles shifted from the original by 0, $\pi/2$, π and $3\pi/2$. Then we calculated the holograms of the form shown in Fig. 5.2 and measured the transmitted intensities corresponding to the calculated holograms. Finally, we used the measured intensities to calculate the angle φ using the curve fitting approach outlined in Section 5.2. This angle is the phase of the transmitted signal. We find that, unlike the case of the intensity control, all the targeted phase values show a small standard deviation of about 10° and the mean values in all the cases are close to the targeted values. Here we note that different regions of interest have different reference signals and phase difference between them is not known. Because of this, for each observation point studied, we decided to take phase value measured corresponding to a targeted phase of 0° as offset and subtract that value from the rest of the measured phase values for that observation point. However, the comments made earlier are valid even if this subtraction is not done.

An ability to simultaneously maximize the intensity at multiple points using the transmission matrix has previously been demonstrated [18]. However, an ability to control each of the multiple points to a specified intensity value has not yet been demonstrated. In Fig. 5.5, we show such a control. Figure 5.5 (a) was captured when the control area was modulated with a phase profile designed to make the region on the right to be brighter, whereas Fig. 5.5 (b) was captured with a phase profile calculated to turn the left area brighter. Both of these phase profiles were calculated following the process similar to the one outlined in Section 5.3.

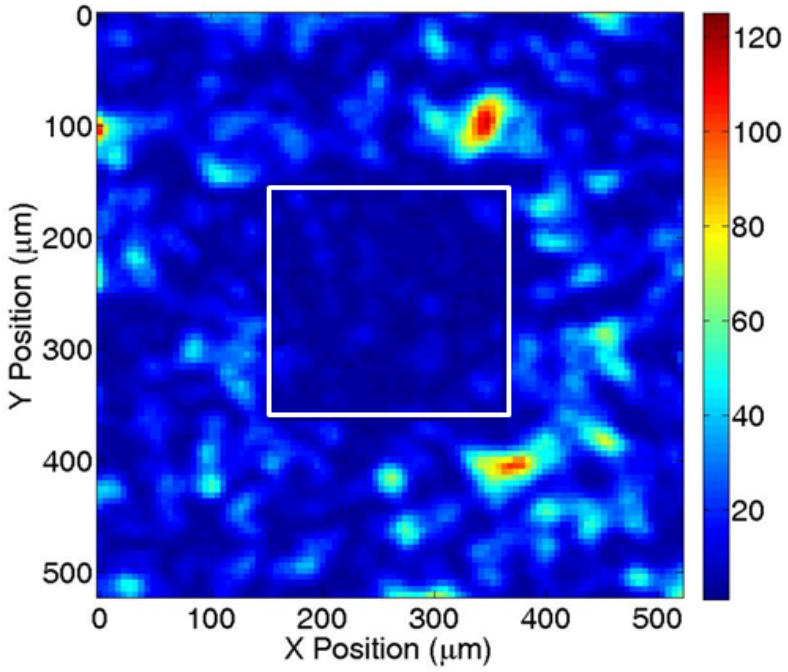

Figure 5.6: Ability to generate extended low intensity areas. Area under control is demarcated by a white rectangle.

We use our ability to control the intensity profile to generate a "homogeneously "low intensity speckle field lying on a region of high intensity speckle field. We show such a field in Fig. 5.6. In the figure, an area of 218.4 μm^2 was targeted to have a low intensity whereas no control was exercised on the rest of the observation plane. The maximum value of intensity in all the areas is 111.5 DN whereas maximum intensity value within the area of interest (AOI) is only 19.5 DN which further decreases to 12.5 DN when only the central portion of the AOI which is half the size of the AOI is considered. This type of control has potential applications in many areas. For example, in 3D photolithography, one might want to avoid exposing the photosensitive polymers to areas where polymerization is to be avoided.

5.5 Conclusion

In this chapter, we presented several interesting developments. At first, we presented a low-cost, phase-only spatial light modulator. The modulator is designed around the Texas Instruments' DLP LightCrafter DMD evaluation module. Spa-

tially dependent phase-only modulation is useful in many interesting studies; however, commercially available modulators are expensive and as a result these components are not widely used in the optics laboratories. The modulator presented here might be useful in rendering spatial phase modulation affordable to all researchers. We used the designed phase modulator in developing techniques to control the transmission of light through highly scattering media. To that end, we presented a novel way of measuring the strength of the reference signal in transmission matrix measurements and demonstrated an ability to control, both the phase and intensity, of the light transmitted through a highly scattering media. These developments prepare us for Chapters 6 and 7 where we present our work on controlling of the polarization of the light transmitted through a highly scattering media.

CHAPTER 6

USING RANDOMNESS AS A RESOURCE IN CONTROLLING POLARIZATION OF LIGHT TRANSMITTED THROUGH RANDOM MEDIA: I

6.1 Introduction

In this chapter, we generalize the concept of the transmission matrix to take into account the polarization of optical fields resulting in the vector transmission matrix (VTM). Further, we outline a method for measuring the absolute values of the VTM elements. It is in contrast to the TM measurements reported in the literature where the TMs have been measured up to a scaling factor [18, 19]. Moreover, we show experimentally that the VTMs can be used to optimize the focus of light through an HSM as well as to predict and control the magnitude of the complex polarization ratio [99], i.e., the ratio of the amplitudes along each polarization basis state of the focused light.

This chapter is organized as follows. In Section 6.2, we present the concept of the VTM and present both the theory and an experimental setup for measuring it. In Section 6.3, we outline a method for optimizing the polarization components of the focused optical field using the VTM. Section 6.4 presents the experimental results and discussion which is followed by the conclusions in Section 6.5. The results presented in this chapter were published in [20]

6.2 Measurement of the vector transmission matrix

It is well known that the effect of multiple scattering is to scramble the polarization of the input field [108]. However, since any polarization state can be represented as a linear combination of two orthogonal basis polarization states [99], to capture the polarization changing behavior of an HSM, it is sufficient to measure components of the output field along each of the basis polarization states as a function of the basis states at the input. Although any set of basis states can be chosen,

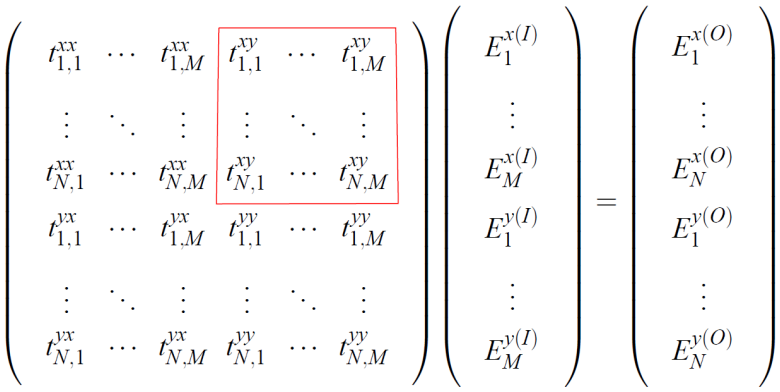

Figure 6.1: A vector transmission matrix relates an optical field incident upon an HSM to the optical field transmitted through the HSM.

here, we take the canonical x and y polarization directions, corresponding to the horizontal and vertical direction in the laboratory reference frame as basis states. Assuming that there are M input degrees of freedom and N observation points, the VTM can be defined to relate the input and output fields as shown in Fig. 6.1.

In Fig. 6.1, $E_m^{i(I)}$ represents the i polarization component at the mth input point with $i = x, y$ and $m = 1$ to M. Similarly, $E_n^{i(O)}$ represents the i polarization component at the nth observation point with $n = 1$ to N. The VTM is of size $2N \times 2M$ and its element $t_{n,m}^{ij}$ gives the contribution of the j polarization component of the field in the mth input state to i polarization component of the field on the nth observation point. The TMs reported in the literature [18, 109] are a subset of the VTM shown in Fig. 6.1. For example, with a y polarized input field incident on an HSM and the analyzer customarily used in the TM measurements [18, 109] at the output oriented along the x direction, the elements of the VTM shown in the box in Fig. 6.1 constitute the scalar TM measured.

Figure 6.2 shows the experimental setup used for VTM measurements. In the figure, a 45°-polarized continuous wave input laser beam is incident upon a non-polarizing beam splitter BS1 thereby creating a reflected and a transmitted beam. The latter then enters a polarizing beam splitter PBS which decomposes the beam into horizontally and vertically polarized components leading to beams B1 and B2, respectively. B1 and B2 are then respectively steered by mirrors M1 and M2 onto a second beam splitter BS 2 which then directs both beams onto a nematic liquid crystal spatial light modulator NLC-SLM. As shown in Fig. 6.2, B1 and B2 are spatially separate on the NLC-SLM which provides independent phase modulation for each of the beams. This spatial separation of the beams is achieved

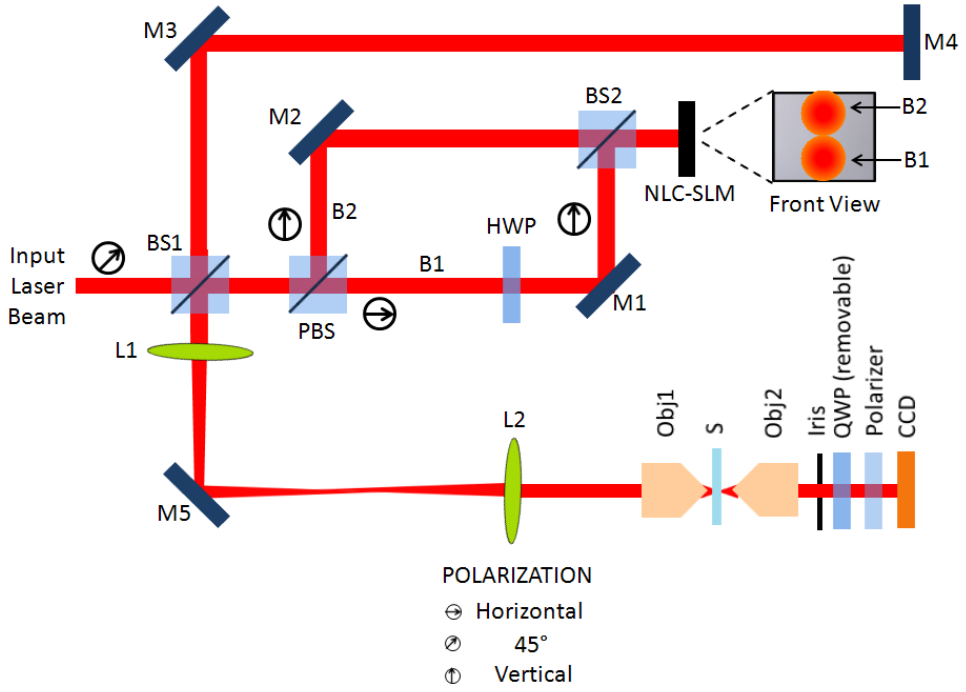

Figure 6.2: Experimental setup to measure the vector transmission matrix.

by walking B2 vertically by tilting PBS and M2 appropriately. Since the NLC-SLM used in our experiments provides phase modulation only for a vertically polarized optical field, B1 is converted to a vertically polarized beam by passing it through a half-wave plate HWP. The surface of the NLC-SLM is then imaged by lens pair L1 and L2 onto the back focal plane of an optical objective Obj1 which focuses the light onto the HSM sample S. The forward scattered optical field is then collected by another objective Obj2, passed through an analyzer P, and subsequently recorded by a CCD camera. This optical field recorded on the CCD is our control signal. The quarter-wave plate QWP shown in the setup is flipped out of the beam path while collecting the VTM elements and flipped into the beam path during polarization measurements. It is worth noting that the component of the scattered light recorded on the CCD that comes from the beam reflected off BS1, steered by M3 and retro-reflected by mirror M4 acts as the reference during VTM measurements. To avoid ambiguity, we define the total reference and total control signals as the reference and control signals that would be recorded by the CCD in the absence of any optical component between Obj2 and CCD.

In our experiments the laser source was an 808-nm diode laser, IQ2C(808-150), acquired from Power Technology, Inc. Although not shown in Fig. 6.2,

the beam coming out of the laser module was expanded, spatially filtered and passed through a half-wave plate-polarizer combination prior to being incident on BS1. The beam splitters BS1, PBS and BS2 with respective part numbers BS013, PBS252 and BS014 were acquired from Thorlabs, Inc. The NLC-SLM is a 512×512 XY series NLC-SLM acquired from Boulder Nonlinear Systems. The HWP, QWP and P were acquired respectively from Karl Lambrecht Corporation, CVI Melles Griot, and Thorlabs, Inc. with respective part numbers MWPQA2-12-V800, QWPO-800-06-4-R10 and LPNIR050-MP. The QWP and P were mounted separately on two PRM1Z8E motorized rotation mount and controller acquired from Thorlabs, Inc. and were controlled through a custom computer code written in MATLAB and LabVIEW. The camera used in our experiments was a Hamamatsu ORCA-285G. The Obj1 was an infinity corrected Spencer $10\times$ objective with an NA, working distance and parfocal distance of 0.25, 9.1 mm and 34 mm. Similarly, Obj2 was an infinity corrected $45\times$ objective from Reichert with an NA, working distance and parfocal distance of 0.66, 0.7 mm and 34 mm, respectively. We studied two types of HSM samples. They were prepared by depositing a ZnO and ethanol mixture, and white nail polish on microscope slides.

To measure the VTM we divide the SLM into 256 segments and use half of the segments to control the x polarized component B1 and the other half to control the y polarized component B2 resulting in 128 input degrees of freedom (DOF) M. Since the contribution of each control segment at the input to an observation point at the output is weak, using the canonical basis results in a low signal-to-noise ratio; therefore we start by measuring the VTM elements using a Hadamard basis at the input [18, 19]. As in [18], we also use four-point phase shifting interferometry. To measure the VTM elements of the form t^{yj}_{n,H_m}, where the subscript H_m in the VTM represents the mth basis element of the Hadamard basis, the analyzer transmission axis is oriented along y, whereas to measure the VTM elements of the form t^{xj}_{n,H_m} the analyzer transmission axis is oriented along x. The VTM elements with Hadamard basis at the input are converted to VTM elements with the canonical elements at the input using a standard Hadamard-to-canonical transformation [107]. These transformed VTM elements are of the form

$$T^{ij}_{n,m} = \sqrt{I^{Ri}_{n,m} I^{Si}_{n,m}} e^{i\triangle\phi}, \tag{6.1}$$

where $I^{Ri}_{n,m}$ and $I^{Si}_{n,m}$ are the i polarization components of the reference and control signals at the nth observation point, respectively, and $\triangle\phi$ is the phase of the

reference signal subtracted from the phase of the control signal. A VTM element should relate the input at the mth input degree of freedom to the output at the nth observation point and as such should be independent of the reference signal; however, as can be seen from Eq. (6.1), the measured VTM elements are scaled by a factor $\sqrt{I^{Ri}_{n,m}}$ which depends on the reference signal. Further, $T^{xj}_{n,m}$ and $T^{yj}_{n,m}$ use the x and y components of the total reference signal as reference in the phase shifting measurements. Since the x and y components of the total reference signal can have a phase difference between them, the measured phase values for $T^{xj}_{n,m}$ and $T^{yj}_{n,m}$ have an offset between them. To use all the VTM elements together this phase offset needs to be corrected.

In our experiments we solve both of these problems by measuring the Stokes vector $\begin{bmatrix} S^{R,0}_{n,m} & S^{R,1}_{n,m} & S^{R,2}_{n,m} & S^{R,3}_{n,m} \end{bmatrix}^\top$ for the total reference signal. The Stokes vector is measured by orientating the polarizer along the x direction and measuring the value of intensity on the CCD as a function of the orientation of the QWP [110]. From the Stokes vector we calculate the x and y components of the total reference signal as [99]

$$I^{Rx}_{n,m} = \frac{1}{2}\left(S^{R,0}_{n,m} + S^{R,1}_{n,m}\right) \tag{6.2}$$

and

$$I^{Ry}_{n,m} = \frac{1}{2}\left(S^{R,0}_{n,m} - S^{R,1}_{n,m}\right), \tag{6.3}$$

respectively. Similarly, the phase angle between the x and y components of the reference signal φ is calculated as [99]

$$\varphi = \frac{1}{2}\angle\left(S^{R,2}_{n,m} + iS^{R,3}_{n,m}\right). \tag{6.4}$$

Using these values the absolute values of the VTM elements are calculated as

$$t^{xj}_{n,m} = \frac{T^{xj}_{n,m}}{\sqrt{I^{Rx}_{n,m}}}, \tag{6.5}$$

and

$$t^{yj}_{n,m} = \frac{T^{yj}_{n,m}}{\sqrt{I^{Ry}_{n,m}}} e^{i\varphi}, \tag{6.6}$$

where we take the phase of the x component of the reference signal as the datum for all of the phases involved in the experiments. As has been shown pre-

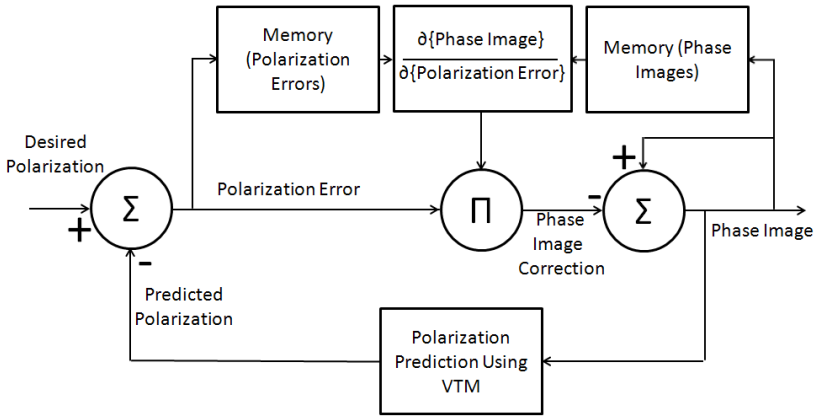

Figure 6.3: A simplified block diagram outlining the procedure followed in calculating the phase image for polarization optimization. A given phase is changed iteratively until the targeted polarization is realized. At each iteration, corrections to the phase image are calculated based on both the nature of the change in polarization error and the phase image from previous iterations.

viously [18, 19], controlling only intensity through the HSM does not require determination of the absolute value of the TM elements. However, for control of the polarization state, it is necessary to be able to tune the relative weights of the polarization components along basis states both in terms of the amplitude and phase, thus knowing the VTM elements to within a scaling factor only is of limited use. In addition, even for intensity only control, knowing the absolute values of the TM or VTM elements can facilitate quantitative control on the intensity, e.g., delivering a specified amount of light to a particular optical mode.

6.3 Phase image calculation for polarization control

The VTM of an HSM captures the medium's polarization changing behavior, and thus it is possible to predict the output polarization given the phase profile at the input. This ability can be used to calculate the phase image to be displayed on the NLC-SLM that can result in the desired polarization components at the output. A conceptual block diagram describing the basic steps in the calculation of the phase image is shown in Fig. 6.3. The process starts with a given phase image. Using the VTM the output polarization for the given phase image is predicted. The error between the desired and the predicted polarization is evaluated and is used to control the correction factor to be applied to the phase image. The nature of the

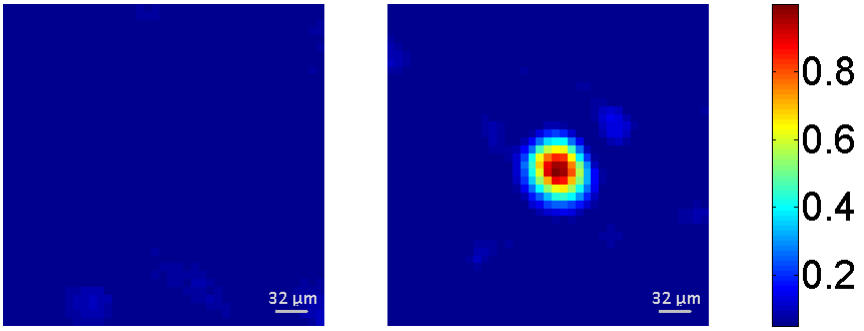

Figure 6.4: Speckle field before and after optimization. An enhancement of 41× was observed with 256 control segments.

change in errors as a function of phase images obtained from previous iterations determines the nature of the correction to be applied to the phase image.

Although Fig. 6.3 illustrates the concept, the actual steps followed in the optimization process are more complicated. Rather than optimizing for the polarization itself, we optimize for the intensity under the constraint that the predicted polarization be close to the desired polarization within a given tolerance limit. In our calculations, we characterize the polarization by the complex polarization ratio defined by two parameters: ϕ and R. These parameters are defined as the difference between the phase and the ratio of the magnitudes of the y and x polarization components, respectively [99]. The optimization problem to be solved is depicted in Eq. (6.7) and is solved by using the *interior point method* available in the KNITRO [111] optimization package accessed from MATLAB. As in any interior or barrier method, KNITRO breaks the optimization problem into a set of barrier sub-problems controlled by a barrier parameter. The algorithm then repeats the process of solving the sub-problem and reducing the barrier parameter until the optimization problem is solved [111].

$$\underset{\angle E_m^{i(I)}}{Maximize}\ I\left(\angle E_m^{i(I)}\right) subject\ to \begin{cases} \left| R^2 - \dfrac{\left|\sum E_n^{y(O)}\right|^2}{\left|\sum E_n^{x(O)}\right|^2} \right| < \varepsilon_r \\ \left(\phi - \angle\sum E_n^{y(O)} + \angle\sum E_n^{x(O)}\right) \mod 2\pi < \varepsilon_p \end{cases} . \tag{6.7}$$

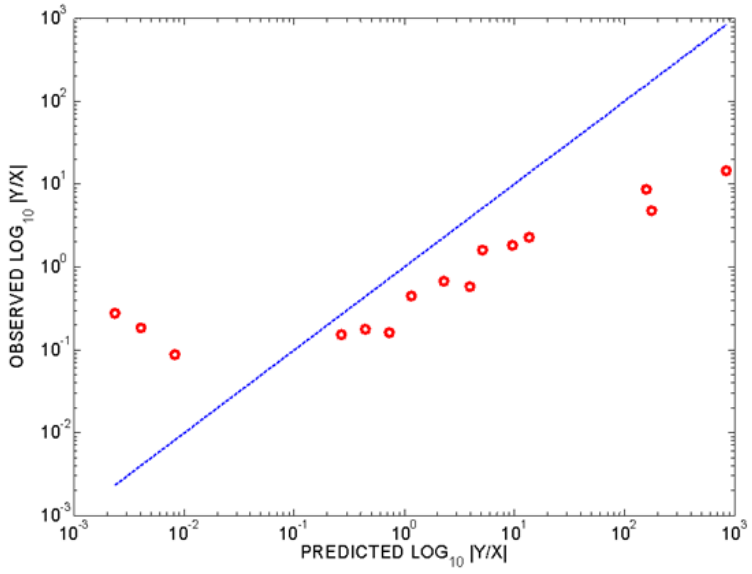

Figure 6.5: Plot of the observed versus predicted polarization state to illustrate the value of the vector transmission matrix in predicting the output polarization state.

6.4 Results and discussion

To elucidate the usefulness of the VTM in predicting the polarization of the light focused through an HSM we carried out a series of experiments. The VTMs were at first measured and then used to design phase images that would focus light through the HSM. Initially, the optimization of the intensity of the focused light was carried out without considering the polarization information contained in the VTMs. Figure 6.4 shows a representative speckle pattern before and after optimization. For 256 control segments on the NLC-SLM, we were able to achieve an intensity improvement of more than 40$\times$ which is consistent with what has been previously reported in the literature using a similar number of control segments [18]; however, for basic polarization studies an improvement by a factor of 10$\times$ was found sufficient. Once the light was focused, the predicted output polarization of the phase image that resulted in the focused light was then calculated by using the VTM and compared with the actual polarization observed.

A scatter plot of the observed versus predicted ratio of the intensities of the y and x polarization components have been plotted in Fig. 6.5. The diagonal line represents the ideal case of equal values of the predicted and the observed ratios and is shown for reference. Any deviation of the observed points from the

diagonal line represents an error in the observed values. From the results we see that the observed ratios follow the predicted ratios to a large extent. The values are especially close for ratios between 0.1 and 10. For these ratios, the average relative error is 66%. Note that when the predicted ratios are too large or small, the observed ratios do not follow the predicted values as faithfully. We expect that this behavior stems from the interplay between the non-ideal experimental conditions, e.g., diffraction at the NLC-SLM, and the stringent requirement on the accuracy of the model of the system when the ratios are too large or small.

Using the procedure outlined in Section 6.3, we calculated the phase images that would result in the ratios of 0.05, 0.5, 1, 2, and 20 for the intensities of the y and x polarization components. These phase images were then displayed on the NLC-SLM to modify the phase profile of the light incident on the HSM. The strength of the x and the y components of the focused light was then measured through the Stokes vector measurement. Due to the fact that our system had a speckle decorrelation time of $\sim$1 hr, the experiments were repeated with different sets of VTMs and different observation points. This is equivalent to repeating the experiment for different samples. In our experiments, speckle decorrelation time was measured by calculating the cross-correlation between measured speckle patterns as a function of time. For each desired ratio, the intensities of the measured x and y polarization components were normalized by the total intensity then plotted on the xy coordinate plane along with the standard deviations along the x and y directions. The results are shown in Fig. 6.6. The targeted values and the trajectory of all possible ratios is also shown for reference. Comparing the targeted and observed values we see that the observed values again follow the targeted ones.

Here we note that in Fig. 6.6 the trajectory of all possible ratios maps an arc of a unit circle in the first quadrant of the xy coordinate plane. Since the ratios of the y and x values change nonlinearly along the circumference of a circle, the plot has a nonlinear scale for the ratios. Moreover, in our experiments the available input degrees-of-freedom was found to be insufficient to control both the relative phase and intensities of the polarization components which limited us to exploring the control of the relative intensities only. Since the relative phases were neglected, each point shown in Fig. 6.6 could represent any point on a unique circle on the Poincaré sphere whereby the locus of a polarization with fixed intensity ratio is a circle normal to the x-axis. The inset in Fig. 6.6 shows a Poincaré sphere with the dashed circle corresponding to an intensity ratio of 1 outlined on it. We are working on modifying the experimental setup to allow for amplitude modulation

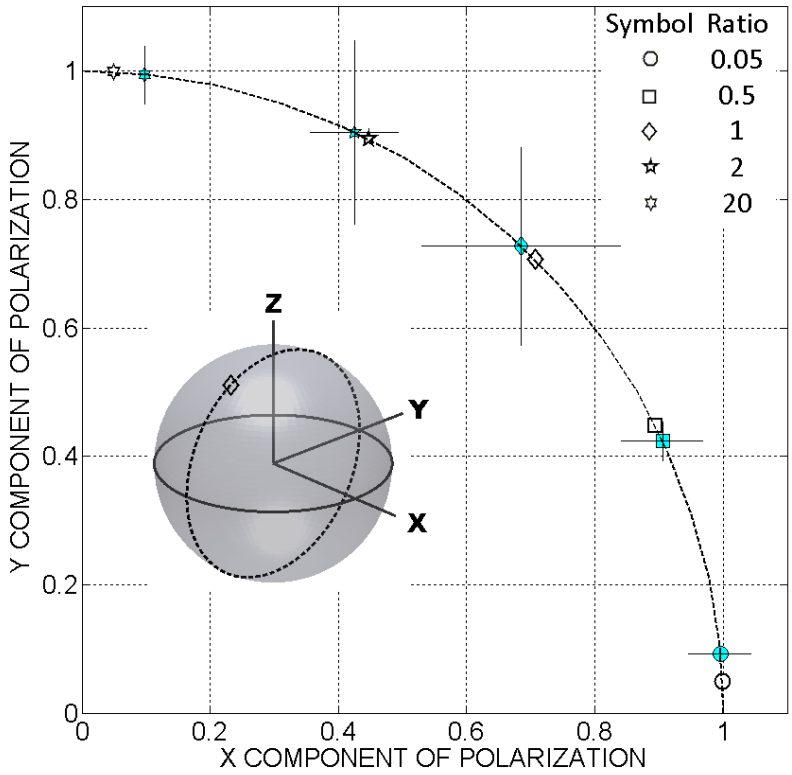

Figure 6.6: Plot comparing the experimentally obtained (closed markers) and targeted (open markers) ratios of the intensities of the polarization components y and x. The dashed curve shows the trajectory of all possible ratios. Each ratio can represent any point on a unique circle on the Poincaré sphere; the inset shows the circle corresponding to the targeted polarization ratio of 1 outlined on the sphere.

at the input which we expect to facilitate finer control over the input field and help us explore the complete state of polarization control of the light focused thorough the highly scattering medium .

6.5 Conclusion

We presented a vector transmission matrix for the study of the polarization behavior of light propagation in highly scattering media. For M input degrees of freedom and N observation points, the size of the vector transmission matrix is $2N \times 2M$, whereas the size for a scalar transmission matrix with the same input degrees of freedom and observation points is $N \times M$. We also discussed a method for experimentally measuring the absolute values of the elements of the vector

transmission matrix. The polarization behavior of the highly scattering media encoded in these elements was shown to be useful in predicting the magnitude of the complex polarization ratio of the light focused through such media. It was further shown that it is possible to calculate a phase profile for the light incident on the highly scattering medium that would deliver the desired magnitude of the complex polarization ratio at the targeted observation point. The ability to predict and control the polarization of the light transmitted through the highly scattering media has potential to be useful in a wide range of imaging, metrology, and fabrication problems.

CHAPTER 7

USING RANDOMNESS AS A RESOURCE IN CONTROLLING POLARIZATION OF LIGHT TRANSMITTED THROUGH RANDOM MEDIA: II

7.1 Introduction

In Chapter 6, we introduced the concept of the vector transmission matrix (VTM). We also demonstrated that the VTM can be used to control the polarization of the light transmitted through a highly scattering medium (HSM). However, after analyzing the elements of the measured VTM, we found that the cross-polarization terms in the VTM are as strong as the other terms. This observation suggests that one should be able to control the polarization of the light transmitted through an HSM even if the field incident on the HSM had only one polarization component. This observation allows us to simplify our optical setup as well as the experimental procedure, and has resulted in a higher experimental stability and a better control over the generated states of polarization (SOPs). We detail these developments in this chapter.

7.2 Measurement of the vector transmission matrix elements

As stated in Section 7.1, to control the polarization of the light transmitted through an HSM it is not necessary to measure all the elements of the VTM. Figure 7.1 shows the VTM elements that are measured in our experiments. We use the optical setup shown in Fig. 7.2 to measure these elements. This setup is similar to the one described in Chapter 5 with two modifications. First, a quarter-wave plate (QWP) is included in the setup. It is mounted on a motorized rotation mount, which itself is fixed on a flip mount. This allows us to flip the QWP into and out of the optical path. Second, a similar motorized rotation mount/flip-mount arrangement is used for the analyzer P as well. These changes allow us to measure the required set of

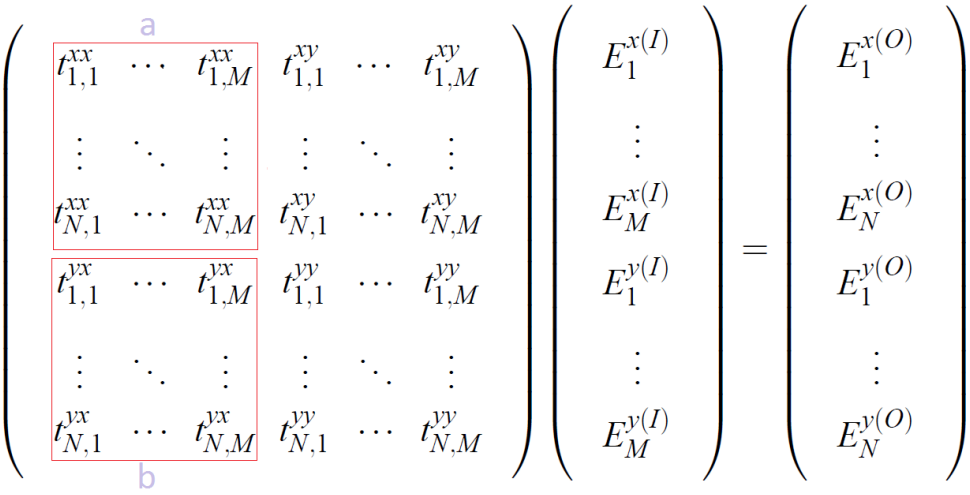

Figure 7.1: A VTM relates the optical field incident on an HSM to the optical field transmitted through it. Multiple scattering taking place inside an HSM results in a transmitted optical field that has components along both of the polarization basis states, even if the incident optical field were polarized along one of the basis states. As a result, to control the polarization of the light transmitted through an HSM, it is enough to measure the elements of the VTM corresponding to only one input polarization state. Here, we demarcate the elements that we measure in our experiments with two (red) boxes. Refer to Section 6.2 for a detailed description of the VTM and the physical meaning of its elements.

VTM elements as well as the SOP of the transmitted light.

To measure the required set of VTM elements, we flip the QWP out of the optical path. At first, we orient the transmission axis of P along the coordinate X axis and measure the transmission matrix elements following the procedure outlined in Section 5.2; this gives us the VTM elements delineated by the box a in Fig. 7.1. We repeat the process with the transmission axis of the P oriented along the coordinate Y axis; this gives us the VTM elements delineated by the box b in Fig. 7.1. As described in Section 6.2 and pointed out by us in [20], the two sets of transmission matrix elements so measured have a phase offset equal to the relative phase between the reference signals used in each case. To correct for this phase offset it is necessary to measure the relative phase between the reference signals used. This can be done by measuring the Stokes vector of the total reference signal. To that end, we flip the QWP into the optical path, turn off the control area on the DMD micro-mirror array (see Section 5.2), and measure the Stokes vector of the transmitted light. From the measured Stokes vector the relative phase φ between the reference signals is calculated. After correcting for the phase offset,

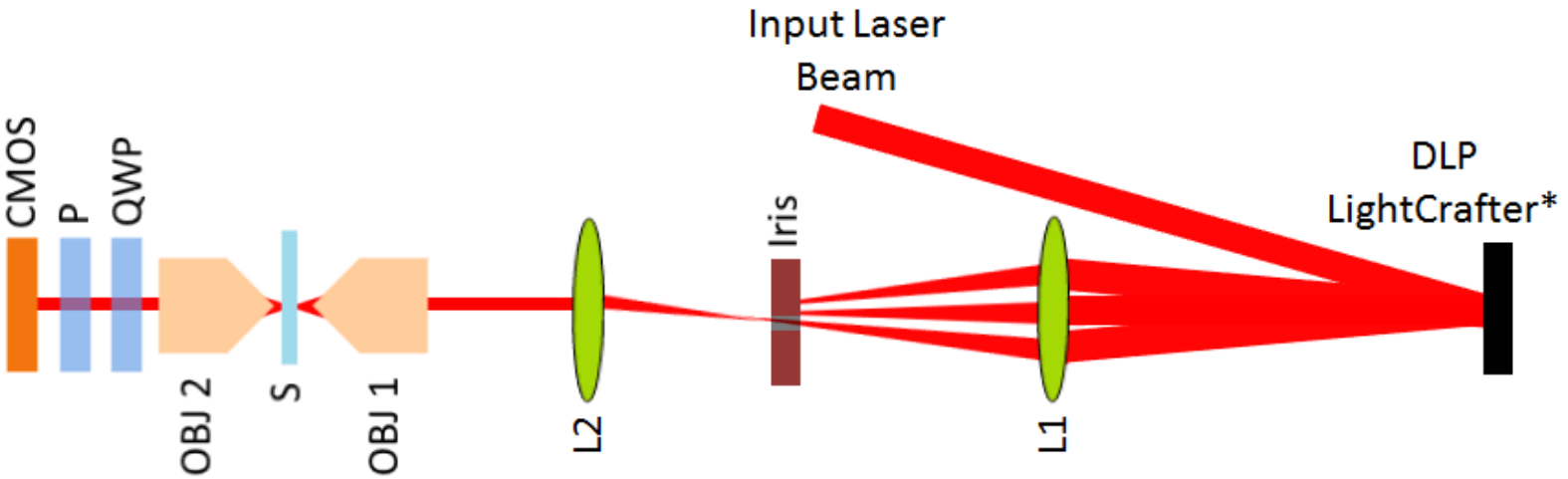

Figure 7.2: Experimental setup to measure the vector transmission matrix.

the form of the measured VTM elements is as follows:

$$t^x_{n,m} = g^x_{nm}\sqrt{I^{C,x}_{n,m}}e^{i\varphi^x_{n,m}} \tag{7.1}$$

and

$$t^y_{n,m} = g^y_{nm}\sqrt{I^{C,y}_{n,m}}e^{i\left(\varphi^y_{n,m}+\varphi\right)}, \tag{7.2}$$

where, Eq. (7.1) describes the VTM elements that govern the x polarized transmitted field. In the equation, g^x_{nm} is the cross-correlation between the x component of the control signal and the reference signal. Similarly, $I^{C,x}_{n,m}$ is the intensity of the x component of the control signal and $\varphi^x_{n,m}$ is the phase difference between the x component of the control signal and the reference signal. The corresponding terms in Eq. (7.2) have similar meanings.

Once the VTM elements are measured, the phase profiles required to achieve the polarization control are calculated using the approach outlined in Section 6.3.

7.3 Results and discussion

7.3.1 Phase offset correction

Here, we briefly illustrate our procedure for phase offset correction. In our experiments, each region of interest is square shaped with 52 μm side length. In Fig. 7.3, we show the magnitude and phase of the vector transmission matrix elements corresponding to the x and y polarized outputs for one region of interest. The phase value in each case was measured with respet to the x and y components of the reference signal. Since these components themselves can have some relative phase, there is phase offset between the phases of the measured vector transmission matrix elements.

To correct for the phase offset, we use a rotating quarter wave plate/fixed analyzer method for measuring the Stokes vector of the reference signal [110] and use the relation between different components of the Stokes vector to calculate the relative phase between the Y and X components of the reference signal.

In Fig. 7.4, we show the data measured for $[1, 0.074, 0.898, -0.397]$. Corresponding phase offset is -23.8°. To correct for this phase offset, this angle is added to the angles shown in Fig. 7.3 (d). This phase offset correction technique

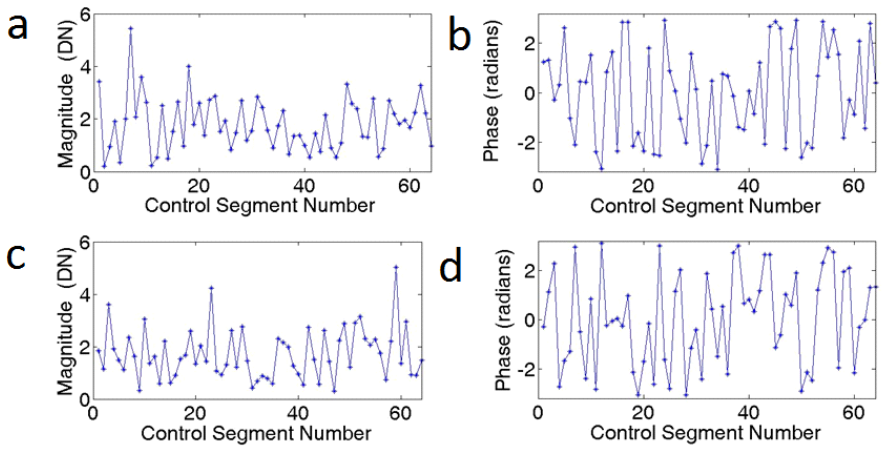

Figure 7.3: Magnitude (a) and (c), and phase (b) and (d) of the transmission matrix elements corresponding to *x* polarized (a) and (b), and *y* polarized (c) and (d) output.

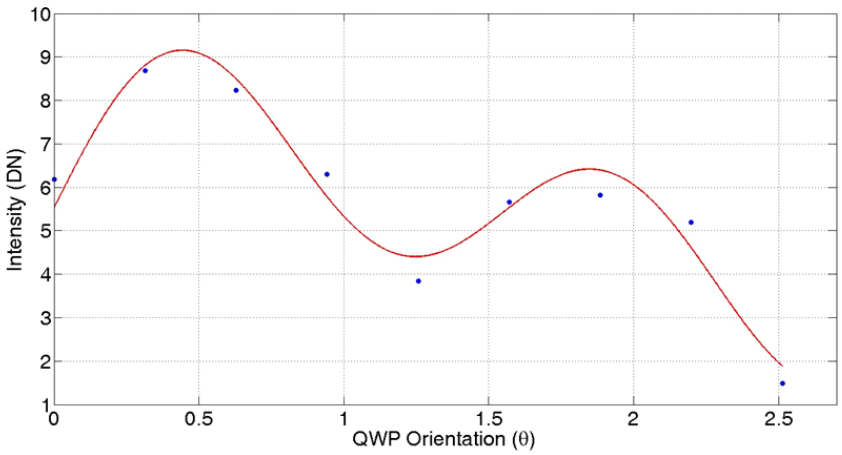

Figure 7.4: An example case of calculation of the relative phase between the *y* and *x* components of the reference signal: the raw measured data (shown by markers) and curve fitted to calculate the Stokes vector are shown. The required relative phase is calculated from the Stokes vector elements.

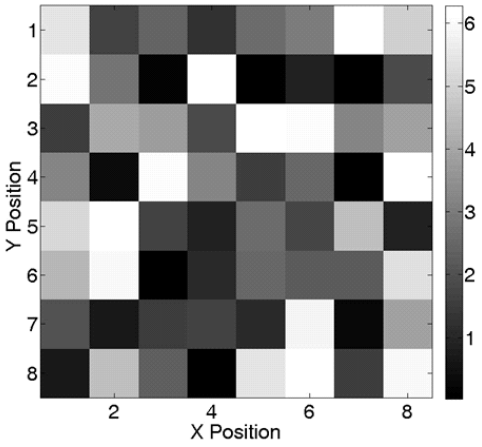

Figure 7.5: A phase profile designed to generated an intensity ratio of 5.828 and phase difference of 90° between the *y* and *x* polarization components of the transmitted field at the region of interest characterized by the VTM elements shown in Fig. 7.3.

is due to us and was reported in the literature as [20].

7.3.2 Phase profile calculation

Once the phase offset corrected absolute values of the vector transmission elements have been measured, corresponding to each polarization control required, a phase profile that would result in that polarization is calculated. For each region of interest we attempt to generate a set of states of polarization and for each polarizatin state required, a different phase profile has to be designed. Corresponding to a desired intensity ratio of 5.828 and phase difference of 90° between the *y* and *x* polarization components for the region of interest for which the transmission matrix elements are shown in Fig. 7.3, the phase profile designed to generate the targeted polarization state is shown in Fig. 7.5. Required phase profiles are imparted to the laser beam incident on the sample by calculating the Lee's hologram (see Section 5.2). The Lee's hologram corresponding to the phase profile shown in Fig. 7.5 is shown in Fig. 7.6.

Once an optical field with the desired phase profile generated, the corresponding state of polarization at the region of interest is measured using the Stokes vector measurement.

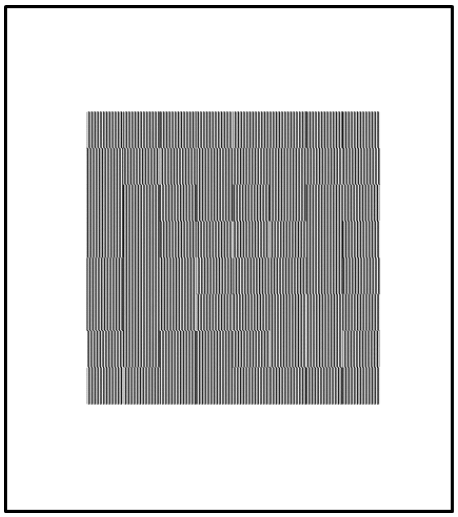

Figure 7.6: The Lee's hologram corresponding to the phase profile shown in Fig. 7.5.

7.3.3 Polarization control

A state of polarization is defined by two parameters: the relative strength R and the relative phase ϕ of the x and y components of the optical field under consideration [99]. So, to check the strength of the control that is availble to us, we attempted to generate the SOPs corresponding to twelve points on the Poincaré sphere. The coordinates of the selected points on the Poincaré sphere and corresponding values of R^2 and ϕ are shown in Table 7.1. These points lie at the intersection of the circles of longitude and circles of latitude drawn in Fig. 7.7 (a).

Our experimental results are shown in Fig 7.7 (b)-(d). In Fig 7.7 (b), we show the results corresponding to the polarization states with a constant targeted latitude of 45°. The plot on the left shows the measured azimuth angles versus the targeted azimuth angles, whereas the plot on the right shows the experimentally observed latitude angles corresponding to each of the targeted azimuth angles. In each case, the solid line represents the ideal values. The results for constant targeted latitude angles of 0° and -45° are similarly shown in Fig. 7.7 (c) and (d), respectively. The degree of control shown in these figures are an improvement over the results presented in Chapter 6 as well as the results presented by us in the literature [20].

However, the results are far from being perfect. Out of the twelve SOPs investigated, for eleven the experimentally observed mean values of the azimuth angles differ from the targeted values by as much as 20°. For the polarization state with the coordinates of $(2\psi, 2\chi) = (45^\circ, 270^\circ)$ the mean value differs from the tar-

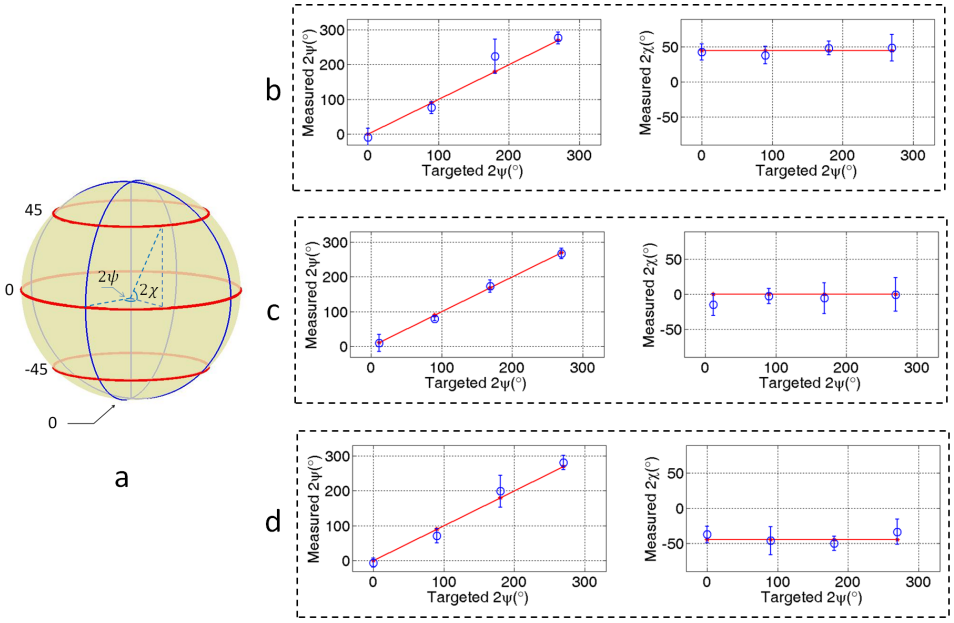

Figure 7.7: Controlling the polarization of the light transmitted through an HSM by using the VTM.

geted by about 43°. Although for the case of the latitude angles the mean values are closer to the targeted values, even there the variation is as much as 15°. These errors are the result of our low fidelity control over R^2. To increase the fidelity it will be necessary to measure the cross-correlation terms between the contributions of different input channels.

7.4 Conclusion

In this chapter, we outlined our modified approach for controlling the polarization of the light transmitted through an HSM. This approach was based on the observation that multiple scattering taking place inside an HSM results in a transmitted optical field that has components along both of the polarization basis states, even if the incident optical field were polarized along one of the basis states. Further, we found the optical setup shown in Fig. 7.2 to be of much help in improving the phase stability in the experiments as unlike the optical setup presented in Chapter 6, it does not involve multiple beam paths. These factors have led us to achieve an improved control over the states of polarization of light that. As pointed out in Section 6.4, we did not have any appreciable control over the relative phase between different polarization components in the past. However, with the cur-

Table 7.1: The parameters of the SOPs generated.

$2\chi\,(^\circ)$	$2\psi\,(^\circ)$	R^2	$\phi\,(^\circ)$
-45	0	0.1716	-90
-45	90	1	-45
-45	180	5.8284	-90
-45	270	1	-135
0	11.4212	0.01	0
0	90	1	0
0	168.5788	100	0
0	270	1	180
45	0	0.1716	-90
45	90	1	-45
45	180	5.8284	-90
45	270	1	-135

rent approach we have a definite control over this phase that is apparent from out ability to generate different states of polarization.

CHAPTER 8

FUTURE WORK

8.1 Vector beam and optical metrology

In Chapter 3 we showed that RAMMP can extract twelve elements of the sample Mueller matrix from a single image. However, a Mueller matrix consists of sixteen elements, and as a result, complete characterization of the linear optical properties using RAMMP still requires two sets of data. One potential avenue of exploration, in this regard, could be to explore the ways to remove this shortcoming. In this regard, it is helpful to remember that RAMMP is limited to twelve elements because the current optical setup acts as an incomplete polarization state detector measuring only three elements of the Stokes vector at a time. One way to improve this would be to design an improved optical setup that provides complete analysis of the state of polarization. This will allow all elements of the Mueller matrix to be measured at once.

The Mueller matrix of a general anisotropic sample is a function of both the azimuth angle and the angle of incidence. However, for a fixed angle of incidence one can relate the Mueller matrices at different azimuth angles by using Mueller matrix transformations for optical elements. RAMMP uses this fact to relate information overlap between intensities recorded for various azimuth angles for a fixed angle of incidence. However, the information overlap between intensities recorded for different angles of incidence is still unexploited. It is likely that combining this information will improve the robustness of the approach. Developing a framework that could enable the use of information contained throughout the field of view would be useful as well.

In Chapter 4 we outlined an approach for measuring the elements of the second-order nonlinear susceptibility tensor of a single nanoparticle. We showed, through simulations, that the approach is robust against noise. However, there are two aspects that need further exploration. First, in any experimental realization, the

nanoparticle under study would have to be on a substrate. As a result, an approach for reliably filtering out the effect of the substrate needs to be developed. An alternative could be to levitate the particle during the measurement process. A second avenue for further study is to simplify the measurement protocol. Currently, our technique requires that the second-harmonic signal emitted by the nanoparticle be interfered with a reference second-harmonic signal. The sole purpose of the interference is to be able to measure the phase and amplitude of the second-harmonic signal emitted by the nanoparticle. It will be interesting to explore the use of non-interferometric techniques of measuring the phase because a need to generate a reference signal and couple it to the experiment is expected to add significantly to the experimental complexity.

8.2 Random media studies

The work done as part of the thesis points to many interesting avenues for further exploration. As noted in Chapters 5-7, the level of control over the intensity, phase and polarization that we have achieved represent an improvement over the state-of-the-art. However, before these controls can be used for any optical metrology, the level of control needs to be improved. We found out through our experiments that contemporary studies in the field have been making an assumption about the coherence of the transmitted light that is not strictly valid; the assumption has been that if a coherent beam is transmitted through a highly scattering medium, at each point on the transmitted field, the contribution of different points on the input field will be coherent to each other. However, we found that the different contributions are not completely coherent. More interestingly, mutual coherence of the contributions seem to vary from complete coherence to incoherence. For a physics point of view, it will be interesting to explore the source of this variation. As we noted in Chapter 5, we do not yet measure all the cross-correlation terms required to accurately predict and hence to control the intensity, phase and polarization of the light transmitted through a highly scattering medium. From an experimental perspective, it will be useful to implement one of the approaches for measuring the cross-correlation terms identified in Chapter 5.

REFERENCES

[1] T. Yoshizawa, Ed., *Handbook of Optical Metrology: Principles and Applications*. New York: CRC Press, 2009.

[2] K. I. Willig, S. O. Rizzoli, V. Westphal, R. Jahn, and S. W. Hell, "STED microscopy reveals that synaptotagmin remains clustered after synaptic vesicle exocytosis," *Nature*, vol. 440, pp. 935–939, 2006.

[3] A. Ahmad, N. D. Shemonski, S. G. Adie, H. S. Kim, W. M. W. Hwu, P. S. Carney, and S. A. Boppart, "Real-time in vivo computed optical interferometric tomography," *Nature Photonics*, vol. 7, pp. 444–448, 2013.

[4] W. Osten, Ed., *Optical Inspection of Microsystems*. New York: CRC Press, 2006.

[5] H. Fujiwara, *Spectroscopic Ellipsometry: Principles and Applications*. West Sussex: John Wiley and Sons Ltd, 2007.

[6] J. Pasquesi, S. Schlachter, M. Boppart, E. Chaney, S. Kaufman, and S. Boppart, "In vivo detection of exercise-induced ultrastructural changes in genetically-altered murine skeletal muscle using polarization-sensitive optical coherence tomography," *Optics Express*, vol. 14, pp. 1547–1556, 2006.

[7] T. Colomb, F. Durr, E. Cuche, P. Marquet, H. G. Limberger, R. P. Salathe, and C. Depeursinge, "Polarization microscopy by use of digital holography: Application to optical-fiber birefringence measurements," *Applied Optics*, vol. 44, pp. 4461–4469, 2005.

[8] C. Abou-Rjeily and A. Slim, "Cooperative diversity for free-space optical communications: Transceiver design and performance analysis," *IEEE Transactions on Communications*, vol. 59, pp. 658–663, 2011.

[9] Y. S. Yeh and D. O. Reudink, "Efficient spectrum utilization for mobile radio systems using space diversity," *IEEE Transactions on Communications*, vol. COM-30, pp. 447–455, 1982.

[10] M. Razavi and J. H. Shapiro, "Wireless optical communications via diversity reception and optical preamplification," *IEEE Transactions on Wireless Communications*, vol. 4, pp. 975–983, 2005.

[11] K. C. Toussaint Jr., S. Park, J. E. Jureller, and N. F. Scherer, "Generation of optical vector beams with a diffractive optical element interferometer," *Optics Letters*, vol. 30, no. 21, pp. 2846–2848, 2005.

[12] C. Maurer, A. Jesacher, S. Furhapter, S. Bernet, and M. Ritsch-Marte, "Tailoring of arbitrary optical vector beams," *New Journal of Physics*, vol. 9, p. 1, 2007.

[13] Q. Zhan, "Cylindrical vector beams: From mathematical concepts to applications," *Advances in Optics and Photonics*, vol. 1, no. 1, pp. 1–57, 2009.

[14] S. C. Tidwell, D. H. Ford, and W. D. Kimura, "Generating radially polarized beams interferometrically," *Applied Optics*, vol. 29, no. 15, pp. 2234–2239, 1990.

[15] M. Bashkansky, D. Park, and F. K. Fatemi, "Azimuthally and radially polarized light with a nematic SLM," *Optics Express*, vol. 18, no. 1, pp. 212–217, 2010.

[16] R. Dorn, S. Quabis, and G. Leuchs, "Sharper focus for a radially polarized light beam," *Physical Review Letters*, vol. 91, no. 23, p. 233901, 2003.

[17] I. M. Vellekoop and A. P. Mosk, "Focusing coherent light through opaque strongly scattering media," *Optics Letters*, vol. 32, no. 16, pp. 2309–2311, 2007.

[18] S. M. Popoff, G. Lerosey, R. Carminati, M. Fink, A. C. Boccara, and S. Gigan, "Measuring the transmission matrix in optics: An approach to the study and control of light propagation in disordered media," *Physical Review Letters*, vol. 104, no. 10, p. 100601, 2010.

[19] D. B. Conkey, A. M. Caravaca-Aguirre, and R. Piestun, "High-speed scattering medium characterization with application to focusing light through turbid media," *Optics Express*, vol. 20, pp. 1733–1740, 2012.

[20] S. Tripathi, R. Paxman, T. Bifano, and K. C. Toussaint Jr., "Vector transmission matrix for the polarization behavior of light propagation in highly scattering media," *Optics Express*, vol. 20, pp. 16 067–16 076, 2012.

[21] C. Stockbridge, Y. Lu, J. Moore, S. Hoffman, R. Paxman, K. C. Toussaint Jr., and T. Bifano, "Focusing through dynamic scattering media," *Optics Express*, vol. 20, pp. 15 086–15 092, 2012.

[22] S. M. Popoff, G. Lerosey, M. Fink, A. C. Boccara, and S. Gigan, "Controlling light through optical disordered media: Transmission matrix approach," *New Journal of Physics*, vol. 13, p. 123021, 2012.

[23] A. P. Mosk, A. Lagendijk, G. Lerosey, and M. Fink, "Controlling waves in space and time for imaging and focusing in complex media," *Nature Photonics*, vol. 6, pp. 283–292, 2012.

[24] M. Kim, Y. Choi, C. Yoon, W. Choi, J. Kim, and Q. H. Park, "Maximal energy transport through disordered media with the implementation of transmission eigenchannels," *Nature Photonics*, vol. 6, pp. 581–585, 2012.

[25] D. J. McCabe, A. Tajalli, D. R. Austin, P. Bondareff, I. A. Walmsley, S. Gigan, and B. Chatel, "Spatio-temporal focusing of an ultrafast pulse through a multiply scattering medium," *Nature Communications*, vol. 2, p. 447, 2011.

[26] O. Katz, E. Small, Y. Bromberg, and Y. Silberberg, "Focusing and compression of ultrashort pulses through scattering media," *Nature Photonics*, vol. 5, pp. 372–377, 2011.

[27] H.-T. Wang, X.-L. Wang, Y. Li, J. Chen, C.-S. Guo, and J. Ding, "A new type of vector fields with hybrid states of polarization," *Optics Express*, vol. 18, pp. 10 786–10 795, 2011.

[28] S. Tripathi and K. C. Toussaint Jr., "Versatile generation of optical vector fields and vector beams using a non-interferometric approach," *Optics Express*, vol. 20, pp. 10 788–10 795, 2012.

[29] O. Weiss and J. Scheuer, "Emission of cylindrical and elliptical vector beams from radial bragg lasers," *Applied Physics Letters*, vol. 97, p. 251108, 2010.

[30] A. Abouraddy and K. C. Toussaint Jr., "Three-dimensional polarization control in microscopy," *Physical Review Letters*, vol. 96, no. 15, p. 153901, 2006.

[31] S. Iwahashi, Y. Kurosaka, K. Sakai, K. Kitamura, N. Takayama, and S. Noda, "Higher-order vector beams produced by photonic-crystal lasers," *Optics Express*, vol. 19, pp. 11 963–11 968, 2011.

[32] S. Vyas, M. Niwa, Y. Kozawa, and S. Sato, "Diffractive properties of obstructed vector Laguerre-Gaussian beam under tight focusing condition," *Journal of the Optical Society of America A*, vol. 28, pp. 1387–1394, 2011.

[33] M. J. Huttunen, M. Erkintalo, and M. Kauranen, "Absolute nonlinear optical probes of surface chirality," *Journal of Optics A*, vol. 11, p. 034006, 2009.

[34] S. Tripathi and K. C. Toussaint Jr., "Rapid Mueller matrix polarimetry based on parallelized polarization state generation and detection," *Optics Express*, vol. 17, no. 24, pp. 21 396–21 407, 2009.

[35] V. G. Niziev and A. V. Nesterov, "Influence of beam polarization on laser cutting efficiency," *Journal of Physics D*, vol. 32, pp. 1455–1461, 1999.

[36] S. Tripathi, B. J. Davis, K. C. Toussaint Jr., and P. S. Carney, "Determination of the second-order nonlinear susceptibility elements of a single nanoparticle using coherent optical microscopy," *Journal of Physics B: Atomic, Molecular and Optical Physics*, vol. 44, no. 1, p. 015401, 2011.

[37] L. Novotny and B. Hecht, *Principles of Nano-Optics*. Cambridge: Cambridge University Press, 2006.

[38] Y. Mushiake, K. Matsumura, and N. Nakajima, "Generation of radially polarized optical beam mode by laser oscillation," *Proceedings of the IEEE*, vol. 60, pp. 1107–1109, 1972.

[39] S. Chandola, K. Hinrichs, M. Gensch, N. Esser, S. Wippermann, W. G. Schmidt, F. Bechstedt, K. Fleischer, and J. F. McGilp, "Structure of Si(111)-in nanowires determined from the midinfrared optical response," *Physical Review Letters*, vol. 102, no. 22, p. 226805, 2009.

[40] J. A. Fagan, J. R. Simpson, B. J. Landi, L. J. Richter, I. Mandelbaum, V. Bajpai, D. L. Ho, R. Raffaelle, A. R. H. Walker, B. J. Bauer, and E. K. Hobbie, "Dielectric response of aligned semiconducting single-wall nanotubes," *Physical Review Letters*, vol. 98, no. 14, p. 147402, 2007.

[41] M. Gilliot, A. E. Naciri, L. Johann, J. J. Stoquert, J. P. Grob, and D. Muller, "Optical anisotropy of shaped oriented cobalt nanoparticles by generalized spectroscopic ellipsometry," *Physical Review B*, vol. 76, no. 4, p. 045424, 2007.

[42] Z. M. Huang, J. Q. Xue, Y. Hou, J. H. Chu, and D. H. Zhang, "Optical magnetic response from parallel plate metamaterials," *Physical Review B*, vol. 74, no. 19, p. 193105, 2006.

[43] W. Wu, E. Kim, E. Ponizovskaya, Y. Liu, Z. Yu, N. Fang, Y. R. Shen, A. M. Bratkovsky, W. Tong, C. Sun, X. Zhang, S. Y. Wang, and R. S. Williams, "Optical metamaterials at near and mid-IR range fabricated by nanoimprint lithography," *Applied Physics A*, vol. 87, no. 2, pp. 143–150, 2007.

[44] M. Losurdo, M. M. Giangregorio, P. Capezzuto, G. Bruno, G. Malandrino, I. L. Fragal, L. Armelao, D. Barreca, and E. Tondello, "Structural and optical properties of nanocrystalline Er_2O_3 thin films deposited by a versatile low-pressure MOCVD approach," *Journal of the Electrochemical Society*, vol. 155, no. 2, pp. G44–G50, 2008.

[45] M. Losurdo, M. Bergmair, G. Bruno, D. Cattelan, C. Cobet, A. de Martino, K. Fleischer, Z. Dohcevic-Mitrovic, N. Esser, M. Galliet, R. Gajic, D. Hemzal, K. Hingerl, J. Humlicek, R. Ossikovski, Z. V. Popovic, and O. Saxl, "Spectroscopic ellipsometry and polarimetry for materials and systems analysis at the nanometer scale: State-of-the-art, potential, and perspectives," *Journal of Nanoparticle Research*, vol. 11, no. 7, pp. 1–34, 2009.

[46] R. A. Chipman, "Polarimetry," in *Handbook of Optics*, M. Bass, E. W. V. Stryland, D. R. Williams, and W. L. Wolfe, Eds. New York: McGraw Hill, Inc., 1995.

[47] D. H. Goldstein, "Mueller matrix dual-rotating retarder polarimeter," *Applied Optics*, vol. 31, no. 31, pp. 6676–6683, 1992.

[48] P. S. Hauge, "Recent developments in instrumentation in ellipsometry," *Surface Science*, vol. 96, no. 1-3, pp. 108–140, 1980.

[49] R. W. Collins and J. Koh, "Dual rotating-compensator multichannel ellipsometer: Instrument design for real-time Mueller matrix spectroscopy of surfaces and films," *Journal of the Optical Society of America A*, vol. 16, no. 8, pp. 1997–2006, 1999.

[50] F. Delplancke, "Automated high-speed Mueller matrix scatterometer," *Applied Optics*, vol. 36, no. 22, pp. 5388–5395, 1997.

[51] F. Delplancke, "Investigation of rough surfaces and transparent birefringent samples with Mueller-matrix scatterometry," *Applied Optics*, vol. 36, no. 30, pp. 7621–7628, 1997.

[52] G. E. Jellison and F. A. Modine, "Two-modulator generalized ellipsometry: Theory," *Applied Optics*, vol. 36, no. 31, pp. 8190–8198, 1997.

[53] G. E. Jellison and F. A. Modine, "Two-modulator generalized ellipsometry: Experiment and calibration," *Applied Optics*, vol. 36, no. 31, pp. 8184–8189, 1997.

[54] E. Compain, B. Drevillon, J. Huc, J. Y. Parey, and J. E. Bouree, "Complete Mueller matrix measurement with a single high frequency modulation," *Thin Solid Films*, vol. 313, pp. 47–52, 1998.

[55] A. De Martino, Y. K. Kim, E. Garcia-Caurel, B. Laude, and B. Drevillon, "Optimized Mueller polarimeter with liquid crystals," *Optics Letters*, vol. 28, no. 8, pp. 616–618, 2003.

[56] J. M. Bueno and P. Artal, "Double-pass imaging polarimetry in the human eye," *Optics Letters*, vol. 24, no. 1, pp. 64–66, 1999.

[57] Y. Jiang, I. Tomov, Y. Wang, and Z. Chen, "Second-harmonic optical coherence tomography," *Optics Letters*, vol. 29, no. 10, pp. 1090–1092, 2004.

[58] T. Yasui, Y. Takahashi, S. Fukushima, Y. Ogura, T. Yamashita, T. Kuwahara, T. Hirao, and T. Araki, "Observation of dermal collagen fiber in wrinkled skin using polarization-resolved second-harmonic-generation microscopy," *Optics Express*, vol. 17, no. 2, pp. 912–923, 2009.

[59] K. Hagimoto and A. Mito, "Determination of the second-order susceptibility of ammonium dihydrogen phosphate and α-quartz at 633 and 1064 nm," *Applied Optics*, vol. 34, no. 36, pp. 8276–8282, 1995.

[60] S. Yazdanfar, L. H. Laiho, and P. T. C. So, "Interferometric second harmonic generation microscopy," *Optics Express*, vol. 12, no. 12, pp. 2739–2745, 2004.

[61] E. Shaffer, N. Pavillon, J. Kuhn, and C. Depeursinge, "Digital holographic microscopy investigation of second harmonic generated at a glass/air interface," *Optics Letters*, vol. 34, no. 16, pp. 2450–2452, 2009.

[62] N. Sandeau, L. L. Xuan, D. Chauvat, C. Zhou, J. F. Roch, and S. Brasselet, "Defocused imaging of second harmonic generation from a single nanocrystal," *Optics Express*, vol. 15, no. 24, pp. 16 051–16 060, 2007.

[63] S. Brasselet, V. L. Floc'h, F. Treussart, J. F. Roch, J. Zyss, E. Botzung-Appert, and A. Ibanez, "In situ diagnostics of the crystalline nature of single organic nanocrystals by nonlinear microscopy," *Physical Review Letters*, vol. 92, no. 20, p. 207401, 2004.

[64] M. Jacobsohn and U. Banin, "Size dependence of second harmonic generation in CdSe nanocrystal quantum dots," *Journal of Physical Chemistry B*, vol. 104, no. 1, pp. 1–5, 2000.

[65] T. Brunhes, P. Boucaud, S. Sauvage, F. Glotin, R. Prazeres, J. M. Ortega, A. Lematre, and J. M. Grard, "Midinfrared second-harmonic generation in p-type InAs/GaAs self-assembled quantum dots," *Applied Physics Letters*, vol. 75, no. 6, pp. 835–837, 1999.

[66] N. Thantu, "Second harmonic generation and two-photon luminescence upconversion in glasses doped with ZnSe nanocrystalline quantum dots," *Journal of Luminescence*, vol. 111, no. 1-2, pp. 17–24, 2005.

[67] E. Delahaye, N. Tancrez, T. Yi, I. Ledoux, J. Zyss, S. Brasselet, and R. Clment, "Second harmonic generation from individual hybrid $MnPS_3$-based nanoparticles investigated by nonlinear microscopy," *Chemical Physics Letters*, vol. 429, no. 4-6, pp. 533–537, 2006.

[68] O. A. Aktsipetrov, P. V. Elyutin, A. A. Fedyanin, A. A. Nikulin, and A. N. Rubtsov, "Second-harmonic generation in metal and semiconductor low-dimensional structures," *Surface Science*, vol. 325, no. 3, pp. 343–355, 1995.

[69] G. W. Bryant and A. Liu, "Second-harmonic generation of semiconductor quantum dots studied by near-field optical microscopy," *Superlattices and Microstructures*, vol. 25, no. 1-2, pp. 361–365, 1999.

[70] J. Erland, S. I. Bozhevolnyi, K. Pedersen, J. R. Jensen, and J. M. Hvam, "Second-harmonic imaging of semiconductor quantum dots," *Applied Physics Letters*, vol. 77, no. 6, pp. 806–808, 2000.

[71] O. A. Aktsipetrov, P. V. Elyutin, A. A. Nikulin, and E. A. Ostrovskaya, "Size effects in optical second-harmonic generation by metallic nanocrystals and semiconductor quantum dots: The role of quantum chaotic dynamics," *Physical Review B*, vol. 51, no. 24, pp. 17 591–17 599, 1995.

[72] A. B. Djurisic and Y. H. Leung, "Optical properties of ZnO nanostructures," *Small*, vol. 2, no. 8-9, pp. 944–961, 2006.

[73] M. Zielinski, D. Oron, D. Chauvat, and J. Zyss, "Second-harmonic generation from a single core/shell quantum dot," *Small*, vol. 5, no. 24, pp. 2835–2840, 2009.

[74] W. L. Chen, T. H. Li, P. J. Su, C. K. Chou, P. T. Fwu, S. J. Lin, D. Kim, P. T. C. So, and C. Y. Dong, "Second harmonic generation tensor microscopy for tissue imaging," *Applied Physics Letters*, vol. 94, no. 18, p. 183902, 2009.

[75] Y. Guan, O. Katz, E. Small, J. Zhou, and Y. Silberberg, "Polarization control of multiply scattered light through random media by wavefront shaping," *Optics Letters*, vol. 37, pp. 4663–4665, 2012.

[76] C. Prada and M. Fink, "Eigenmodes of the time reversal operator: A solution to selective focusing in multiple-target media," *Wave Motion*, vol. 20, no. 2, pp. 151–163, 1994.

[77] I. M. Vellekoop, E. G. van Putten, A. Lagendijk, and A. P. Mosk, "Demixing light paths inside disordered metamaterials," *Optics Express*, vol. 16, no. 1, pp. 67–80, 2008.

[78] S. Popoff, G. Lerosey, M. Fink, A. C. Boccara, and S. Gigan, "Image transmission through an opaque material," *Nature Communications*, vol. 1, no. 6, p. 81, 2010.

[79] I. M. Vellekoop, A. Lagendijk, and A. P. Mosk, "Exploiting disorder for perfect focusing," *Nature Photonics*, vol. 4, no. 5, pp. 320–322, 2010.

[80] I. Moreno, J. A. Davis, T. M. Hernandez, D. M. Cottrell, and D. Sand, "Complete polarization control of light from a liquid crystal spatial light modulator," *Optics Express*, vol. 20, pp. 364–376, 2011.

[81] A. Safrani and I. Abdulhalim, "Liquid-crystal polarization rotator and a tunable polarizer," *Optics Letters*, vol. 34, no. 12, pp. 1801–1803, 2009.

[82] G. Milione, H. I. Sztul, D. A. Nolan, and R. R. Alfano, "Higher-order Poincaré sphere, Stokes parameters, and the angular momentum of light," *Physical Review Letters*, vol. 107, no. 5, p. 053601, 2011.

[83] I. J. Hodgkinson and Q. H. Wu, *Birefringent Thin Films and Polarizing Elements*. World Scientific Publishing Co. Pte. Ltd., 1997.

[84] C. Brosseau, "Interaction of radiation with linear media," in *Fundamentals of Polarized Light: A Statistical Optics Approach*. New York: John Wiley and Sons, Inc., 1998.

[85] D. E. Aspnes, "Expanding horizons: New developments in ellipsometry and polarimetry," *Thin Solid Films*, vol. 455-456, pp. 3–13, 2004.

[86] B. Richards and E. Wolf, "Electromagnetic diffraction in optical systems. ii. Structure of the image field in an aplanatic system," *Proceedings of the Royal Society of London. Series A*, vol. 253, no. 1274, pp. 358–379, 1959.

[87] W.-Q. Zhang, "New phase shift formulas and stability of waveplate in oblique incident beam," *Optics Communications*, vol. 176, no. 1-3, pp. 9–15, 2000.

[88] R. M. A. Azzam and N. M. Bashara, "Reflection and transmission of polarized light by stratified planar structure," in *Ellipsometry and Polarized Light*. Amsterdam: North Holland, 1989.

[89] D. W. Berreman, "Optics in stratified and anisotropic media: 4x4 matrix formulation," *Journal of Optical Society of America*, vol. 62, pp. 502–510, 1972.

[90] H. Fujiwara, "Ellipsometry of anisotropic materials," in *Spectroscopic Ellipsometry: Principles and Application*. West Sussex: John Wiley and Sons Ltd, 2007.

[91] M. Iwanaga, "Effective optical constants in stratified metal-dielectric metameterial," *Optics Letters*, vol. 32, pp. 1314–1316, 2007.

[92] Z. Liu, H. Lee, Y. Xiong, C. Sun, and X. Zhang, "Far-field optical hyperlens magnifying sub-diffraction-limited objects," *Science*, vol. 315, p. 1686, 2007.

[93] A. Salandrino and N. Engheta, "Far-field subdiffraction optical microscopy using metamaterial crystals: Theory and simulations," *Physical Review B*, vol. 74, p. 075103, 2006.

[94] B. J. Davis and P. S. Carney, "Robust determination of the anisotropic polarizability of nanoparticles using coherent confocal microscopy," *Journal of the Optical Society of America A*, vol. 25, no. 8, pp. 2102–2113, 2008.

[95] P. P. De Vries, D. V. V. Coevorden, and A. Lagendijk, "Point scatterers for classical waves," *Reviews of Modern Physics*, vol. 70, no. 2, pp. 447–466, 1998.

[96] R. Boyd, *The Nonlinear Optical Susceptibility*. San Diego: Academic Press, 2003.

[97] C. A. Dailey, B. J. Burke, and G. J. Simpson, "The general failure of Kleinman symmetry in practical nonlinear optical applications," *Chemical Physics Letters*, vol. 390, no. 1-3, pp. 8–13, 2004.

[98] L. Le Xuan, S. Brasselet, F. Treussart, J. F. Roch, F. Marquier, D. Chauvat, S. Perruchas, C. Tard, and T. Gacoin, "Balanced homodyne detection of second-harmonic generation from isolated subwavelength emitters," *Applied Physics Letters*, vol. 89, no. 12, p. 121118, 2006.

[99] B. E. A. Saleh and M. C. Teich, *Fundamentals of Photonics*. Hoboken, NJ: John Wiley and Sons, Inc, 2007.

[100] B. J. Davis, S. C. Schlachter, D. L. Marks, T. S. Ralston, S. A. Boppart, and P. S. Carney, "Nonparaxial vector-field modeling of optical coherence tomography and interferometric synthetic aperture microscopy," *Journal of the Optical Society of America A*, vol. 24, no. 9, pp. 2527–2542, 2007.

[101] P. N. Buther and D. Cotter, *The Elements of Nonlinear Optics*. Cambridge: Cambridge University Press, 2003.

[102] C.-T. Tai, *Dyadic Green Function in Electromagnetic Theory*. Piscataway: Institute of Electrical and Electronics Engineers, 1994.

[103] S. M. Kay, *Fundamentals of Statistical Signal Processing: Estimation Theory*. Upper Saddle River, NJ: Prentice Hall, 1993.

[104] R. Leitgeb, C. K. Hitzenberger, and A. F. Fercher, "Performance of Fourier domain vs. time domain optical coherence tomography," *Optics Express*, vol. 11, no. 8, pp. 889–894, 2003.

[105] *DLP®LightCrafter™ Evaluation Module (EVM): User's Guide*, Texas Instruments, 2013.

[106] W. H. Lee, "Binary synthetic holograms," *Applied Optics*, vol. 13, pp. 1677–1682, 1974.

[107] R. C. Gonzalez and R. E. Woods, *Digital Image Processing*. Hoboken, NJ: Prentice Hall, 2007.

[108] A. Dolginov, Y. Gnedin, and N. Silant'ev, "Photon polarization and frequency change in multiple scattering," *Journal of Quantitative Spectroscopy and Radiative Transfer*, vol. 10, no. 7, pp. 707–754, 1970.

[109] S. M. Popoff, A. Aubry, G. Lerosey, M. Fink, A. C. Boccara, and S. Gigan, "Exploiting the time-reversal operator for adaptive optics, selective focusing, and scattering pattern analysis," *Physical Review Letters*, vol. 107, no. 26, 2012.

[110] B. Schaefer, E. Collett, R. Smyth, D. Barrett, and B. Fraher, "Measuring the Stokes polarization parameters," *American Journal of Physics*, vol. 75, no. 2, pp. 163–168, 2007.

[111] R. H. Byrd, J. Nocedal, and R. A. Waltz, "KNITRO: An integrated package for nonlinear optimization," in *Large Scale Nonlinear Optimization*, G. D. Pillo and F. Giannessi, Eds. New York: Springer Verlag, 2006, pp. 35–59.